The uncertainties in the laboratory-measured short-wave refractive indices of mineral dust aerosols and the derived optical properties: A theoretical assessment

Senyi Kong[1], Zheng Wang[1], Lei Bi[1]

[1]Key Laboratory of Geoscience Big Data and Deep Resource of Zhejiang Province, School of Earth Sciences, Zhejiang University, Hangzhou, 310027, China

Correspondence to: Lei Bi (bilei@zju.edu.cn)

Abstract. Mineral dust particles are typically nonspherical and inhomogeneous; however, they are often simplified as homogeneous spherical particles for retrieving the refractive indices from laboratory measurements of scattering and absorption coefficients. This study theoretically investigated uncertainties in refractive indices and corresponding optical properties resulting from this simplification at various sizes within the wavelength range of 355 to 1064 nm. Different numerical experiments were conducted under both ideal and realistic scenarios, taking into account instrumental bias in the realistic scenarios. In the numerical experiments, the inhomogeneous super-spheroid models were considered as the dust samples, while the homogeneous super-spheroid models and sphere models were used to retrieve the refractive indices. Under the ideal scenario, the look-up tables for the homogeneous super-spheroid models satisfactorily covered the measurements at any size and wavelength, while those for the sphere models failed when considering large sizes. Under the realistic scenario, both the homogeneous super-spheroid models and sphere models were ineffective for large sizes due to discrepancies in size distribution resulting from the measurements using an optical particle counter. Nevertheless, it was possible to retrieve the imaginary parts of the refractive indices based solely on the absorption coefficients. The imaginary parts obtained from the sphere models were generally consistent with those from the super-spheroid models under ideal conditions, while the former was significantly smaller than the latter under the realistic conditions. In addition, the retrieved imaginary parts were found to be size-dependent, which could be attributed to the inherent limitations of homogeneous models in characterizing inhomogeneous particles. Results showed that the uncertainties in the imaginary part and single scattering albedo should be smaller than 0.002 (0.0007) and 0.03 (0.01), respectively, under conditions of high (low) absorption. The sphere models tended to overestimate the asymmetry factor. The uncertainty in the asymmetry factor exhibited a significant variation, reaching up to 0.04 or even larger. Nonetheless, the uncertainties in the phase matrices resulting from the uncertainties in refractive indices were generally acceptable within a specific model.

1 Introduction

Dust aerosols, one of the most dominant aerosols globally, play a crucial role in regulating the energy budget of the Earth's
30   climate system through direct, semi-direct, and indirect radiative effects (Ackerman et al., 2000; Atkinson et al., 2013; Hansen
et al., 1997; Kinne et al., 2006; Takemura et al., 2000). However, accurately describing the radiative effect of dust aerosols
requires quantitative information about their shape, size distribution, and mineralogical composition, which still have large
uncertainties (Adebiyi et al., 2023b; Di Biagio et al., 2020; Kok et al., 2023; Stegmann and Yang, 2017; Wang et al., 2020).
Tremendous efforts have been devoted to developing nonspherical models for dust simulation (Bi et al., 2009, 2010, 2018a;
35   Dubovik et al., 2006; Kahnert, 2015; Kalashnikova and Sokolik, 2004; Kemppinen et al., 2015a; Lin et al., 2018; Lindqvist et
al., 2014; Mishchenko et al., 1997; Saito et al., 2021). Among these models, the homogeneous super-spheroid dust models
have shown good agreement with laboratory measurements of scattering matrices and have demonstrated excellent
performance in simulating polarized satellite measurements and airborne light detection and ranging (LiDAR) observations
(Kong et al., 2022; Lin et al., 2018, 2021). In addition, inhomogeneous super-spheroid models have been developed using the
40   newly updated invariant imbedding T-matrix (IITM) method (Wang et al., 2023).

The size distributions of dust aerosols from various sources under different conditions (transport or near sources) have been
widely investigated in a large number of laboratory measurements and field campaigns (Adebiyi et al., 2023a; Jeong, 2020;
Kandler et al., 2009; Müller et al., 2011; Reid et al., 2003; Ryder et al., 2018; Tegen and Fung, 1994). However, an inherent
ambiguity exists in the sizing of the dust particles (Reid et al., 2003). Most recently, Huang et al. (2021) reported that laboratory
45   measurements by optical particle counters could underestimate the geometric diameter of dust aerosols with coarse sizes
mainly due to the spherical assumption of dust particle shape.

Complex refractive indices (RI), which are fundamentally determined by the mineralogical composition of dust, play a critical
role in calculating dust optical properties. The real parts (n) indicate the ratio of the speed of light in a vacuum to its speed in
the medium, while the imaginary parts (k) denote the attenuation of light in the medium, which characterizes its absorptivity.
50   It should be noted that the short-wave refractive indices of dust were normally retrieved from the extinction (or scattering) and
absorption coefficients measured in the laboratory. In many retrievals, the heterogeneous and irregular dust aerosols are
simplified to homogeneous spherical particles, as calculating electromagnetic scattering by nonspherical particles is
challenging, especially for large sizes (Di Biagio et al., 2017b, 2019; McConnell et al., 2010; Müller et al., 2009; Petzold et
al., 2009; Ryder et al., 2013). However, ample evidence has demonstrated that assuming a spherical shape leads to significant
55   biases in the optical properties of irregular dust aerosols (Dubovik et al., 2000; Mishchenko et al., 2000). Therefore, it is
necessary to quantify the uncertainties associated with the resulting dust refractive indices obtained based on the assumption
of homogeneous spherical particles.

Several studies have utilized spheroid models to obtain the refractive indices of irregular dust aerosols. Dubovik et al. (2000)
examined the bias of such an assumption during retrieval of the optical properties for nonspherical dust particles from Aerosol
60   Robotic Network (AERONET) sun and sky radiance measurements. They considered realistic dust aerosols represented by

spheroid models. However, the retrieval of the real parts of the refractive indices failed in most cases, while the imaginary parts could only be obtained with relatively large uncertainties under certain circumstances when using the Lorenz-Mie theory. Wagner et al. (2012) set the real parts of the refractive indices to 1.53 and retrieved the imaginary parts of Saharan soil samples from laboratory measurements of the extinction and absorption coefficients using a spheroid model. The derived imaginary

65 parts were then used to evaluate the imaginary parts generated by the effective medium approximations. Similarly, Rocha-Lima et al. (2018) retrieved the imaginary parts of the fine-mode Saharan dust using the sphere and spheroid models at wavelengths of 350 to 2500 nm and assuming a constant value of 1.56 for the real parts. However, uncertainties in the refractive indices resulting from the model shapes were not resolved, as the results for two samples in that study were contradictory. In addition, there are still morphological differences between the spheroid models and the realistic nonspherical dust particles.

70 For instance, Sorribas et al. (2015) used the spheroid models to simulate the scattering and backscattering coefficients of dust aerosols and compared them with the laboratory observations. While the spheroid models, in contrast to the sphere models, produced results that were closer to the observations, the computed scattering coefficients were nearly 49% smaller than the observed values. Kemppinen et al. (2015) investigated the reliability of the tri-axial ellipsoid models for retrieving the refractive indices from the scattering matrices, by considering the irregular inhomogeneous models as the actual dust particles.

75 Nevertheless, a systematic quantification of uncertainties in laboratory measurements of dust refractive indices due to the spherical assumption is always lacking (Di Biagio et al., 2019).

Assessing such uncertainties of laboratory experiments of the dust samples is challenging. It is nearly impossible to find a model that precisely matches the morphology of the actual dust aerosols; thus, uncertainties regarding shape equivalence always exist. On the other hand, the true values of the optical properties of dust samples are still unknown. It is difficult to

80 evaluate the extent to which the homogeneous models can accurately reproduce the true values using the retrieved refractive indices, as realistic dust particles are rarely homogeneous.

However, these uncertainties can be easily investigated through numerical experiments that consider the inhomogeneous super-spheroid dust models as realistic representations of dust aerosols. In this paper, our objective is to revisit the laboratory measurements of refractive indices of mineral dust at short wavelengths and conduct a comprehensive theoretical analysis of

85 the associated uncertainties. In addition, we also investigate the consistency in optical properties between realistic dust aerosols and homogeneous models.

This paper is organized in four sections. In Sect. 2, we describe the experimental design, including the overall procedure, the models and computational methods used, the numerical measurements and the retrieval methods. Section 3 presents the results and discussions. The uncertainties of the dust refractive indices obtained in the laboratory, based on the assumption of

90 homogeneous spherical particles, are investigated at different sizes and wavelengths. The corresponding optical properties are then calculated from the retrieved refractive indices and compared to the true values. Following this discussion, we describe the extent to which these theoretical uncertainties might manifest in a real laboratory setting. Finally, a summary is provided in Sect. 4.

2 Experimental design

2.1 Overall procedure

95

We conducted a numerical experiment at five specific wavelengths (355, 532, 633, 865, 1064 nm) to assess the uncertainties in the dust refractive indices resulting from assuming a homogeneous spherical morphology. Figure 1 illustrates a flowchart outlining the steps involved in the numerical experiment, which consisted of four procedures:

1. Dust samples of different sizes and optical databases for homogeneous models were prepared. Inhomogeneous super-
100   spheroid dust models were regarded as the "dust samples" and the corresponding optical property database was calculated for different size parameters. The optical databases for the homogenous sphere and homogeneous super-spheroid models for different size parameters were also established.

2. Size distribution, absorption coefficients, and scattering coefficients of the "dust samples" were measured. The size distribution was artificially assumed, after which the absorption and scattering coefficients could be calculated
105   accordingly.

3. A look-up table for the refractive indices of dust particles was established. The size distribution of the "dust samples" was used (with or without correction) to calculate the absorption and scattering coefficients of both homogeneous dust models (sphere and super-spheroid).

4. The refractive indices of the "dust samples" were retrieved. The absorption and scattering coefficients of the "dust
110   samples" were located in the look-up table, and the corresponding refractive indices were determined. The Bouguer–Lambert method was also introduced for comparison.

In accordance with laboratory studies (Di Biagio et al., 2019), four instruments were used: Aethalometer, Nephelometer, scanning mobility particle sizer (SMPS) and Optical Particle Counter (OPC) (Figure 1; SMPS is not shown). Two correction processes were considered for the measurements of "dust samples" to mimic actual laboratory experiments. The OPC is
115 typically used to measure the scattering intensity of individual particles and provides the diameter of the standard non-absorbing sphere model (polystyrene latex spheres, RI = 1.59+0i), which has equivalent scattering intensity (Heim et al., 2008). However, the absorption of dust aerosols and the non-sphericity of the models (namely, super-spheroid) can introduce bias to the measured size distribution. Therefore, the size distribution measured using the OPC needs to be corrected before being used to establish a look-up table (Di Biagio et al., 2017; Huang et al., 2021; see Sect. 2.3.1). The other correction is related to
120 the measurements of scattering coefficients. The Nephelometer measures the scattering coefficients between 7 and 170° due to difficulties in measurements in the forward $(0 - 7^o)$ and backward $(170 - 180^o)$ directions. Hence, a scattering truncation correction is needed to convert them into the scattering coefficients for the entire field of view $(0 - 180^o$; see Sect. 2.3.2). Four experiments were designed to represent four scenarios with or without size correction and scattering truncation correction (Table 1). Note that E1 represents an ideal situation in which no instrumental defects need to be corrected for the measurements,
125 while E4 is the closest to the real laboratory experiment.

Table 1: A brief description of the four experiments. "Without correction" denotes that no biases existed in the measurements, whereas "With correction" assumes an instrumental bias in the measurements and then corrects the bias based on previous studies.

Experiment		scattering truncation correction	
		Without	With
size correction	Without	E1	E2
	With	E3	E4
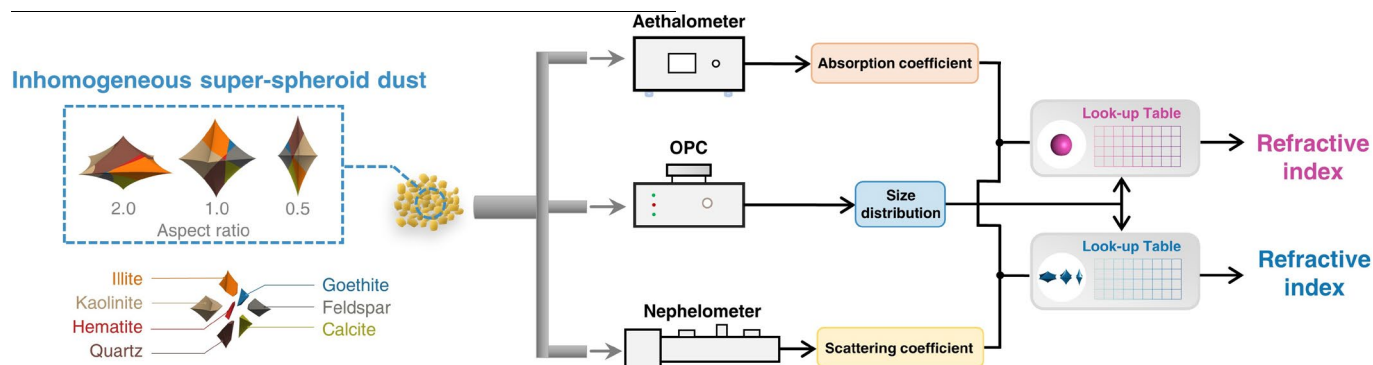
Figure 1: A flowchart for the numerical experiment.

2.2 Model and computational method

The super-spheroid models were developed for modelling atmospheric aerosols, including dust, sea salt, and ice crystals (Bi et al., 2018b; Li et al., 2022; Lin et al., 2018; Sun et al., 2021). The equation for the super-spheroid model can be written as shown below:

$$\left(\frac{x}{a}\right)^{2/e} + \left(\frac{y}{a}\right)^{2/e} + \left(\frac{z}{c}\right)^{2/e} = 1, \tag{1}$$

in which a and c are the lengths of the semi-major axes along the corresponding coordinate axes, and e is the roundness parameter. Specifically, a/c was defined as the aspect ratio. In this study, the value of e was fixed at 2.5, a value based on previous studies (Kong et al., 2022; Lin et al., 2018, 2021). Additionally, three aspect ratios (0.5, 1.0, 2.0) were considered, and the mean values of their optical properties were utilized to describe dust particles for both the inhomogeneous and homogeneous super-spheroid models. The size parameter was defined as $\pi D_m/\lambda$, in which D_m indicates the length of the longest axis of the particle, and λ is the wavelength. Optical properties are directly related to the size parameter instead of only the D_m. We calculated the single particle optical properties using the IITM method for inhomogeneous super-spheroid models (Bi et al., 2013; Bi and Yang, 2014; Wang et al., 2023). The calculations were performed at size parameters ranging from 0.1 to 80 and wavelengths of 355, 532, 633, 865, and 1064 nm. Note that the maximum size parameter was extended to 100 for wavelengths of 355 and 532 nm. This extension ensures that large particles at short wavelengths can be accurately characterized. For homogeneous super-spheroid models, an optical database ranging from size parameter 0.1 to 1000 was developed. The IITM method was used for size parameters varying from 0.1 to 50, while the improved geometric optics method

(IGOM) was applied for size parameters ranging from 50 to 1000 (Bi and Yang, 2017; Yang and Liou, 1996). Note that the IITM method is a rigorous algorithm, whereas the IGOM method is suited for the geometric-optics domain. However, the accuracy of the IGOM method and the effectiveness of combining these two methods were examined and validated in several

150   studies (Bi et al., 2009; Bi and Yang, 2014; Lin et al., 2018; Yang et al., 2007). The uncertainties caused by the calculation of optical properties are negligible compared to those in experiments. To reduce the computational burden, the neural network developed by Yu et al. (2022) was used. The single particle optical properties of sphere models were calculated using the Lorenz–Mie theory (Bohren and Huffman, 2008). In the optical database for homogeneous sphere and super-spheroid models, the real part of the refractive index ranges from 1.40 to 1.70 at intervals of 0.01, while the imaginary part varies from 0.0001

155   to 0.015 at steps of 0.0001.

The "dust samples" are represented by the inhomogeneous super-spheroid models (Figure 1). This inhomogeneous model is based on previous evidence that suggests the presence of polymineralic aggregates in dust samples (Jeong and Nousiainen, 2014; Lindqvist et al., 2014). The mineralogy of dust samples from various sources is presented by Di Biagio et al. (2017). We choose the sample from Algeria for our study because it has a medium iron content, which is believed to be representative

160   of the global average. Previous evidence has reported that the mineralogical composition varies with particle sizes (Kandler et al., 2007, 2009). However, for the purposes of this study, we assume that the composition is size-independent in order to simplify the question and investigate the effects of morphology. The mineral composition consists of 45.1% kaolinite, 21.5% quartz, 18.3% illite, 7.9% feldspar, 4.4% calcite, 1.4% goethite, and 1.4% hematite by mass concentration.

The refractive indices of several major mineral components are shown in Figure 2. It is evident that hematite and goethite

165   exhibit the highest absorption at short wavelengths. The clays, including chlorite, illite, kaolinite, and montmorillonite, have similar refractive indices due to their similar chemical compositions. Quartz, on the other hand, has negligible absorption. The refractive indices of goethite, as reported by Bedidi and Cervelle (1993), are only available for wavelengths ranging from 460 to 700 nm. Unfortunately, no other reported values are available for reference. It is worth noting that the refractive indices of goethite are similar to those of magnetite, particularly in terms of the imaginary parts. Therefore, we adopted the refractive

170   indices of magnetite as an alternative for goethite for wavelengths below 460 nm and above 700 nm. The current reported values of hematite refractive indices have large uncertainties (Go et al., 2022). However, the general trends and magnitudes among these refractive indices at the five selected wavelengths are relatively close. In our numerical experiments, we assumed the refractive indices of various minerals used in this study to be accurate. It is important to mention that these experiments were conducted theoretically and did not involve any actual measurement values. Therefore, the accuracy of the refractive

175   indices of the minerals had little influence on our analysis.
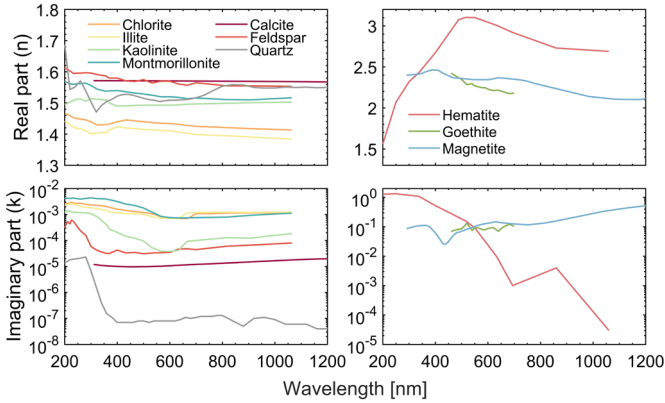
Figure 2: The refractive indices (RI) of various minerals at the wavelengths of 200 to 1200 nm. The RIs of calcite are obtained from the work of Roush (2021); The RIs of chlorite are obtained from the work of Lee et al. (2020); the RIs of feldspar, illite, kaolinite, and montmorillonite are obtained from the work of Egan and Hilgeman (1979); The RIs of hematite are obtained from the work of Longtin et al. (1988); The RIs of quartz are obtained from the work of Khashan and Nassif (2001); The RIs of goethite are obtained from the work of Bedidi and Cervelle (1993), and the RIs of magnetite are obtained from the work of Querry (1987).

2.3 Measurements

2.3.1 Size distribution

In the numerical experiments, the size distribution of dust was "measured" following the method described by Di Biagio et al. (2019). The OPC was used to measure the scattering intensity from individual particles at specific wavelengths within a defined range of scattering angles ($\theta_{min} - \theta_{max}$), which could be expressed as shown below:

$$I_{sca} = \frac{1}{2}I_0 C_{sca} \int_{\theta_{min}}^{\theta_{max}} P(\theta)sin\theta d\theta \ . \tag{2}$$

I_{sca} represented the scattering intensity, I_0 represented the incident intensity of the OPC light source, C_{sca} represented the scattering cross section, $P(\theta)$ represented the phase function, and θ denoted the scattering angle. The experiments considered two types of OPC. One was the skyGrimm OPC (referred to as GRIMM), which operated at a wavelength of 655 nm and covered an angular range from 30° to 150° (Bundke et al., 2015). The other one was the WELAS OPC (referred to as WELAS), which used a 4200K white light Xenon arc lamp and a 90° scattering angle (Heim et al., 2008). Given a specific model, the scattering intensity was tabulated as a function of the size parameter of a single particle theoretically, and then the size of a realistic particle could be determined once the scattering intensity was measured. Normally, the diameter of a polystyrene latex sphere (RI = 1.59+0i) is given by the OPC, which is referred as the optical diameter (D_{opt}). The conversions from the optical diameter measured using the OPC to the geometric diameter (D_{geo}) of various models were conducted (Figure 3a, b). The geometric diameter represented the diameter of a volume-equivalent sphere. Prior values of refractive indices were needed for the conversions. The real parts of the refractive indices (n) for the homogeneous models were set to 1.47, 1.50, and 1.53, while the imaginary parts (k) varied from 0.001 to 0.005 in 0.001 increments based on the values provided by Di Biagio et al. (2019). Besides, the SMPS was used for D_{geo} values smaller than 0.3μm, the GRIMM was used for 0.3 μm < D_{geo} ≤

1 µm, and the WELAS was used for $D_{geo} > 1$ µm (Di Biagio et al., 2019). The D_{geo} as "measured" by the SMPS did not need to be converted among the models with different shapes because the detection values were directly related to the particle mass instead of optical properties. Note that the conversions were different for the GRIMM and WELAS due to the differences in the range of scattering angles and the wavelength of the light source. The significance of the differences in the phase function decreased when integrated over a wide angular range (Mishchenko et al., 1997). Hence, the conversions for the sphere and super-spheroid models were more similar for the GRIMM than for the WELAS. Nevertheless, the D_{geo} for the super-spheroid models were smaller than those for the sphere models.

The conversions between the D_{geo} for the sphere models and that for the super-spheroid models were illustrated in Figure 3c, d. Note that the D_{geo} for the sphere models were nearly comparable to the D_{geo} for both the inhomogeneous and homogeneous super-spheroid models when D_{geo} was smaller than 1 µm. However, the D_{geo} of the super-spheroid models were significantly overestimated when assuming the sphere models for relatively large sizes. This overestimation was also indicated by Huang et al. (2021). The conversion factors (C_f), defined as $D_{geo,super-spheroid}/D_{geo,sphere}$, were found to be smaller than 0.5 at 10 µm. The C_f values for the inhomogeneous models were approximately 8% smaller than those for the homogeneous models. Besides, the inhomogeneous models showed similar trends to the low-absorbing homogeneous models in which $k = 0.001$ (Figure 3a, b). Sensitivity studies showed that the conversions were far less sensitive to n than to k (not shown). The inappropriate prior values of k led to biases in the converted particle size between the homogeneous models and inhomogeneous models.
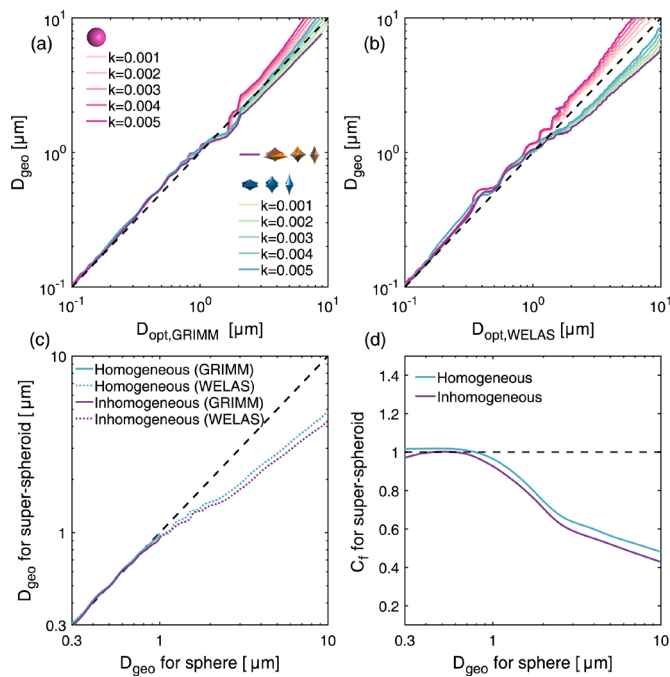
Figure 3: The conversions among the optical diameters (D_{opt}) measured by the optical particle counters of GRIMM and WELAS, the geometrical diameters (D_{geo}) obtained from the homogeneous sphere models, the homogeneous super-spheroid models and the

inhomogeneous super-spheroid models. Panels (a) and (b) display the geometrical diameters (D_{geo}) obtained from different models and compared to the optical diameters measured by the optical particle counters of GRIMM and WELAS. The real part (n) of the refractive index for the homogeneous models is 1.50 and the imaginary part (k) varies from 0.001 to 0.005. Panel (c) illustrates the D_{geo} conversions from the sphere models to the homogeneous and inhomogeneous super-spheroid models, while Panel (d) shows the
225 **corresponding conversion factors (C_f). The mean values of the conversion results are illustrated for which n = 1.47, 1.50, 1.53 and k = 0.001, 0.002, 0.003, 0.004, and 0.005 are chosen for the homogeneous models.**

The "measured" particle number size distributions in the four experiments were adopted from the five-modal lognormal size distributions reported by Di Biagio et al. (2019) and displayed in Figure 4. Each model considered three size distributions representing small (S), medium (M), and large (L) particles, respectively. The small size distribution represented mode 1, the
230 medium size distribution included modes 1–3, and the large size distribution consisted of all five modes (Table 2). Note that the size distributions were assumed to be the same for all the models in experiments E1 and E2, while they varied among models in experiments E3 and E4 due to corrections.

To closely resemble actual laboratory conditions, the size distributions for spherical models in E3 and E4 were initially set to be the same as those for the Algerian dust samples measured by Di Biagio et al. (2019). Then, the size distributions for the
235 super-spheroid models were converted accordingly. Note that in E1 and E2, the size distribution at the large size (L) was smaller than that in E3 and E4. This was done to ensure that all databases of the various models could encompass 99.9% of the cumulative distribution function of the volume size distributions. This approach was taken because the focus of this study was not to compare different experiments, but rather to examine the uncertainties within each experiment. The size conversions can be expressed as shown below:

240
$$\frac{dN}{dD_{geo}} = \frac{dN}{dD_{geo,sphere}} \cdot \frac{dD_{geo,sphere}}{dD_{geo}} = \frac{dN}{dD_{geo,sphere}} \cdot \left(\frac{1}{C_f} - \frac{D_{geo} \cdot \frac{dC_f}{dD_{geo}}}{C_f^2} \right), \tag{3}$$

in which $D_{geo} = D_{geo,sphere} \cdot C_f$, representing the geometrical diameter for the inhomogeneous or homogeneous super-spheroid models. For a specific size parameter, the D_{geo} for super-spheroids were smaller than those for spheres.
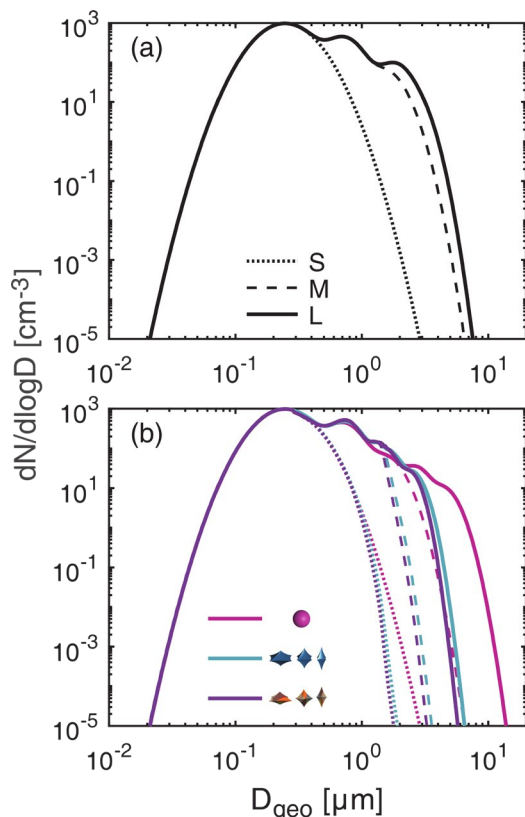
Figure 4: The size distributions in E1/E2 (a) and E3/E4 (b).

245 **Table 2: The parameters for the five-modal lognormal size distributions for sphere models in the experiments. N indicates the number of concentrations (unit: cm^{-3}), D_g represents the geometric mean (unit: μm), and σ_g denotes the geometric standard deviation (unitless).**

Experiments	Mode 1			Mode 2			Mode 3			Mode 4			Mode 5		
	N	D_g	σ_g	N	D_g	σ_g	N	D_g	σ_g	N	D_g	σ_g	N	D_g	σ_g
E1/E2	267	0.29	1.50	207	0.77	1.30	65	1.60	1.30	37	1.96	1.20	26	2.48	1.24
E3/E4	267	0.29	1.50	207	0.77	1.30	65	1.60	1.30	37	2.80	1.20	26	4.50	1.25

2.3.2 Scattering and absorption coefficients

250 The scattering and absorption coefficients were "measured" using the Nephelometer (TSI Inc. model 3563) and Aethalometer (Magee Sci. AE31 model), respectively. An angular truncation existed in the Nephelometer, which could only be used to measure the scattering coefficients between 7 and 170° ($\beta_{sca}(\theta_7 - \theta_{170})$) due to the limits of the instrument. To obtain the scattering coefficients for the entire field of view ($\beta_{sca}(\theta_0 - \theta_{180})$), a scattering truncation correction was needed. The scattering coefficients for an angular range from θ_{min} to θ_{max} can be expressed as shown below:

255
$$\beta_{sca}(\theta_{min} - \theta_{max}) = \frac{1}{2} \int_{D_{geo,min}}^{D_{geo,max}} \int_{\theta_{min}}^{\theta_{max}} P(D_{geo}, \theta) \cdot sin\theta \cdot C_{sca}(D_{geo}) \cdot \frac{dN}{dD_{geo}} d\theta dD_{geo}.$$ (4)

Hence, $\beta_{sca}(\theta_0 - \theta_{180})$ could be easily obtained by multiplying $\beta_{sca}(\theta_7 - \theta_{170})$ by the truncation factor (C_{trunc}). C_{trunc} was calculated based on the equation shown below:

$$C_{trunc} = \beta_{sca,model}(\theta_0 - \theta_{180})/\beta_{sca,model}(\theta_7 - \theta_{170}).$$ (5)

In E1 and E3, we made the assumption that the $\beta_{sca}(\theta_0 - \theta_{180})$ could be directly "measured" by the instrument. However, in

260 E2 and E4, the $\beta_{sca}(\theta_0 - \theta_{180})$ was corrected from $\beta_{sca}(\theta_7 - \theta_{170})$. Prior values of the refractive indices were also needed for calculating the C_{trunc}. The values of *n* were fixed at 1.53, while *k* was set to 0.004, 0.003, 0.001, 0.002, and 0.003 at 355, 532, 633, 865, and 1064 nm, respectively. These values were adopted from the study by Di Biagio et al. (2019) and modified based on the absorptivity of the "dust samples". Sensitivity tests showed that a variation of 0.001 in *k* resulted in a 0.4% variation in C_{trunc}, while a variation of 0.03 in *n* resulted in only a 0.1% variation in C_{trunc}. Thus, it was believed that the

265 uncertainties caused by the prior values of the refractive indices were small. Generally, C_{trunc} varied in the range of 1.1 to 1.7, and increased with size but decreased with wavelength. The differences in C_{trunc} between the super-spheroid models and the sphere models were approximately 1.5% at the large size (L) in E1 and E2. Such small differences were also reported by Sorribas et al. (2015). It was reasonable to observe such a difference because the influence of shape on the phase function was less significant when integrated over the size distribution. However, such differences were large (up to approximately 25%) at

270 large sizes in E3 and E4 due to the large differences in the corrected size distributions.

Actually, the Aethalometer (Magee Sci. AE31 model) did not directly measure absorption coefficients but rather attenuation coefficients (Hansen et al., 1984). Extensive efforts have been made to determine the absorption coefficients by accounting for corrections related to scattering, loading, and multiple scattering effects, using the attenuation and scattering coefficients (Arnott et al., 2005; Collaud Coen et al., 2010; Di Biagio et al., 2017a; Schmid et al., 2006; Virkkula et al., 2007; Weingartner

275 et al., 2003). The corrections for dust particles were validated using measurements from the Multi-Angle Absorption Photometer (MAAP) and Cavity Attenuated Phase Shift Extinction (CAPS) (Di Biagio et al., 2017a). Therefore, we assumed no bias in the absorption coefficient measurements for all four experiments.

2.4 Retrieval method

2.4.1 Look-up table: exact and range values

280 The root mean square deviation (RMSD) of the scattering coefficients and the absorption coefficients were calculated for various refractive indices in the look-up table at each wavelength and size, following the methods in previous studies (Di Biagio et al., 2019; Wagner et al., 2012). The formula can be expressed as shown below:

$$RMSD(X, \lambda, n, k) = \sqrt{\left(\frac{\beta_{sca}(X, \lambda, n, k) - \beta_{sca,model}(X, \lambda, n, k)}{\beta_{sca,model}(X, \lambda, n, k)}\right)^2 + \left(\frac{\beta_{abs}(X, \lambda, n, k) - \beta_{abs,model}(X, \lambda, n, k)}{\beta_{abs,model}(X, \lambda, n, k)}\right)^2}.$$ (6)

11

The variable X represents the size and can be either S, M, or L. The minimum value of RMSD indicates the refractive indices

285 with the best agreement. Due to the sparse nature of the measurements, it was almost impossible for them to fall on the grid points of the look-up tables. Hence, the four refractive indices corresponding to the four smallest values of RMSD were averaged. These average refractive indices were referred to as the exact values.

Di Biagio et al. (2019) provided an estimation of the uncertainty in the scattering and absorption coefficients. They found that the relative uncertainty in the scattering coefficients ranged 5% to 12%, while, for the absorption coefficients, it ranged from

290 22% to 30% at 370 nm and 23% to 87% at 950 nm. In this study, we assumed a relative uncertainty of 8% in the scattering coefficients and 30% in the absorption coefficients. By considering these uncertainties, we were able to obtain the range of possible refractive indices. However, if the "measurements" were not covered within the range of the look-up table, the retrieved refractive indices were discarded. It is worth noting that the "measured" absorption coefficients were always within the range of the look-up table, as shown in Figure 5. Therefore, we also demonstrated the potential range of imaginary parts

295 by solely considering the absorption coefficients. In this study, we did not consider the Kramers–Kronig relationship between n and k, as we only obtained the refractive indices at five wavelengths.

2.4.2 Bouguer–Lambert method

The Bouguer–Lambert method was frequently used in earlier studies (Patterson et al., 1977; Sokolik et al., 1993; Volz, 1972) to determine k based on the absorption coefficient. By considering the space containing dust aerosols and air as a homogeneous

300 medium, the value of k can be derived using the equation shown below:

$$k = \frac{\lambda \beta_{abs,medium}}{4\pi},$$ (7)

in which $\beta_{abs,medium} = \beta_{abs}/V_{dust}$, and V_{dust} denoted the volume of the ensemble of dust particles. The advantage of this method is that it eliminates the need for any optical calculations. However, a disadvantage is that it may not provide accurate results due to unrealistic assumptions. Nonetheless, this method can still be used for comparison purposes.

305 ## 3 Results and discussion

3.1 The retrieved refractive indices in E1/E2

Figure 5 illustrates the "measured" scattering and absorption coefficients, as well as the look-up tables for the super-spheroid models and sphere models in experiments E1 and E2. Note that the general shapes of the look-up tables shrank as the size increased. At a small size (Figure 5c), both the ranges of the look-up tables for the super-spheroid and sphere models could

310 cover the "measurements", while the range for the sphere model barely matched the "measurements" at a large size (Figure 5a). This finding is consistent with previous studies that have shown a large discrepancy between the measured scattering coefficients and the calculated counterparts due to the non-sphericity of large particles (Schladitz et al., 2009). Therefore, n is typically fixed at a specific value, such as 1.53, in the retrieval of the refractive indices (Müller et al., 2009; Schladitz et al.,

2009; Wagner et al., 2012). However, the absorption coefficients were always within the range of both look-up tables. The
315 influence of the scattering truncation correction on the scattering coefficients increased with size. For a small size, the
correction was nearly negligible. Note that the exact "measurements" exceeded the range of the look-up tables for the super-
spheroid models at large sizes and at wavelengths of 355 and 532 nm when considering such a correction. The uncertainty
range of the scattering coefficients was large compared to the range of the look-up tables. At a large size, n could vary from
1.40 to 1.70 within the uncertainty. Accurately retrieving n was challenging. However, in an ideal scenario, the
320 "measurements" could fall within the range of the look-up tables, and the corresponding refractive indices could be retrieved
at any size, when the "dust samples" and the models had the same size distribution and shape.

Note that the ambiguous definition of size for irregular particles could also lead to discrepancies between the "measurements"
and the simulations based on the sphere models (Chen et al., 2011). Saito and Yang (2022) suggested that the effective radius,
defined as three times the volume divided by four times the average projected area, was the most appropriate size descriptor
325 for non-spherical particles. However, we found that the discrepancies were even larger when the effective radius was used (not
shown). The effective radius was smaller than the geometric radius at the same size parameter for the super-spheroid model.
As a result, the simulated scattering coefficients of the sphere models using the effective radius were even smaller than those
using the geometric radius.
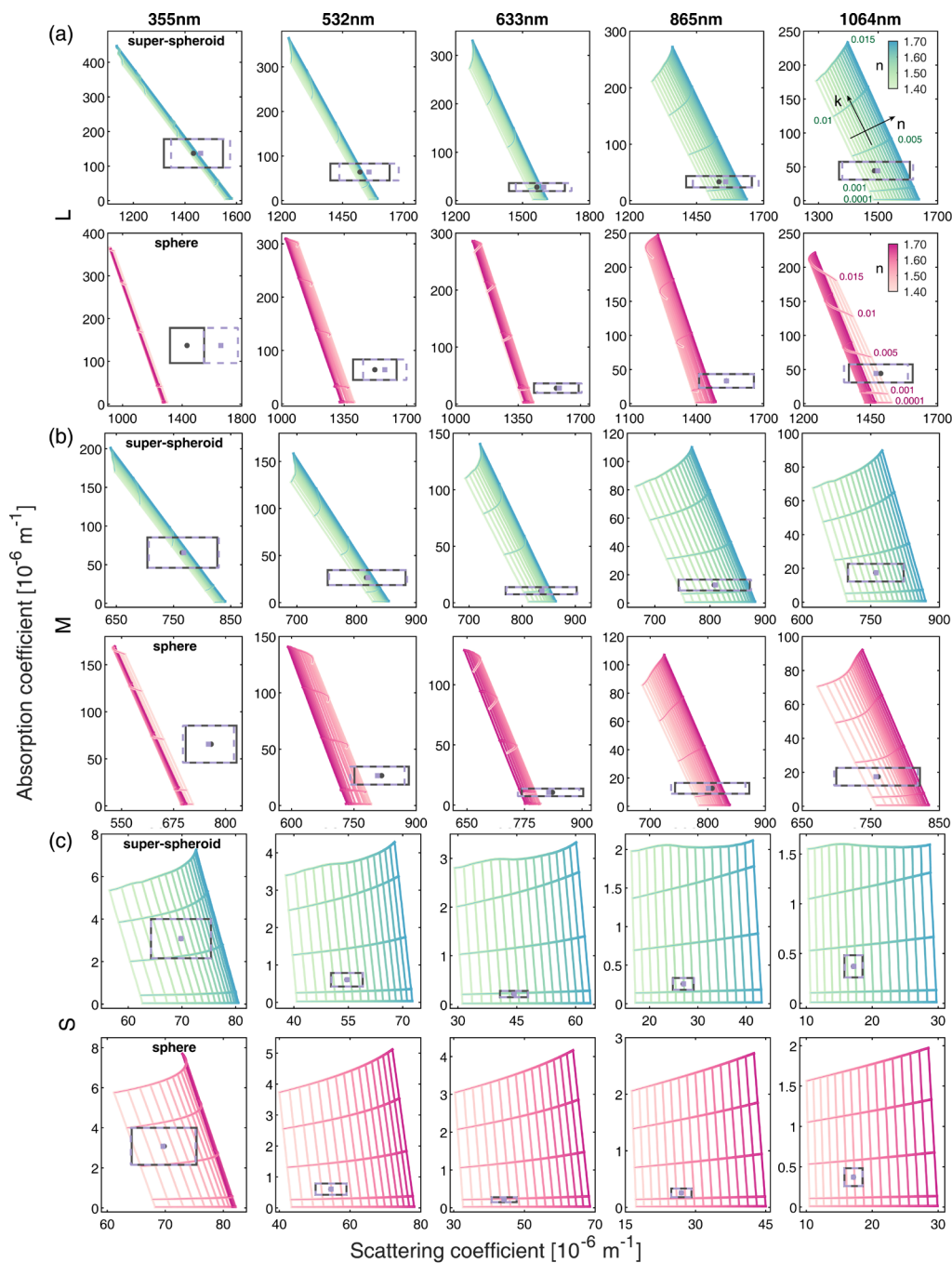
Figure 5: The lookup tables for refractive indices produced by the sphere model and super-spheroid model with different particle sizes (S, M, L in (a), (b), and (c), respectively) to determine the absorption coefficient versus the scattering coefficient for E1/E2. The black round point and rectangle denote the exact "measurement" and its corresponding uncertainties whereas the light purple square point and rectangle with dashed line denote the "measurement" and its corresponding uncertainties after truncation correction. In the lookup table, the real parts (n) are represented by different colors, and five values of the imaginary parts (k) (0.0001, 0.001, 0.005, 0.01, and 0.015) are displayed.

14

The "measured" absorption coefficients exhibited a decrease with increasing wavelength until reaching a minimum value at a wavelength of 633 nm, beyond which they increased (Figure 6a). Consequently, this trend was also observed in the imaginary parts of the refractive index, which displayed a similar bow-shaped signature (Figure 6c). This behaviour could be attributed to the imaginary parts of goethite. Note that we adopted the refractive indices of magnetite as an alternative for goethite at

340 wavelengths of above 700 nm due to the lack of direct measurements. At these longer wavelengths, the absorptivity of dust was mainly determined by goethite, as hematite exhibited weak absorption (Go et al., 2022). Hence, the absorptivity increased with wavelengths above 633 nm.

Rocha-Lima et al. (2018) conducted a study on Saharan dust and derived k across a range of wavelengths from 350 to 2500 nm. Their findings also showed a bow-shaped signature of k, with a minimum value observed at approximately 650 nm for

345 fine-mode particles. However, the increasing trend of the absorption coefficients ranging from 633 to 1064 nm and the bow-shaped signature of k were not consistently observed in many actual laboratory measurements (Di Biagio et al., 2019; Müller et al., 2009, 2011; Wagner et al., 2012). While some studies indeed have demonstrated a bow-shaped signature of k, but the absorptivity of dust either weakened or remained unchanged below 1064 nm (Balkanski et al., 2007; Wells et al., 2012). Therefore, it is possible that the imaginary parts of goethite may have been overestimated above 700 nm by assuming the k of

350 magnetite. Accurate measurement of the refractive indices of goethite at shorter wavelengths are still required.

Given that the retrieved refractive indices in experiments E1 and E2 were similar, and the differences could be deduced from Figure 5, we only displayed the results for E1 in Table 3. Note that in Figure 6b and c, the exact retrieved refractive indices for the super-spheroid models were available at all sizes, while those for the sphere models were only available at a small size and partly available at a medium size. Generally, no obvious regulations were found in the real parts at different sizes but a

355 clear decreasing trend with size was observed for the imaginary parts. It could be deduced that simulating the optical properties of the inhomogeneous models using a homogeneous model and a single refractive index was nearly impossible, as the homogeneous models could not accurately represent them. The phenomenon that different refractive indices might be obtained for particles of varying sizes was also noted in the laboratory measurements (Orofino et al., 1998).
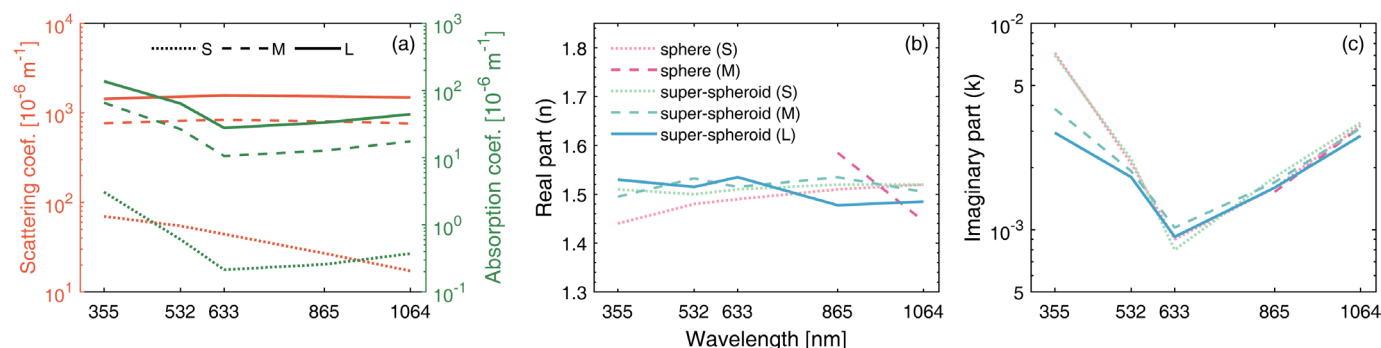
360 **Figure 6: The scattering coefficients and absorption coefficients of the "measurement" (a) and the exact refractive indices retrieved from the homogeneous sphere models and the homogeneous super-spheroid models (b, c) for different particle sizes (S, M, L) for E1.**

Figure 7 displays the range values of k for the super-spheroid and sphere models, as well as their differences in E1. The k obtained through the Bouguer–Lambert method was not influenced by the models in E1, as the volume size distributions were

365 the same for all the models. Note that the k obtained through the Bouguer-Lambert method were substantially larger than those retrieved by the look-up table. This finding could be attributed to the unrealistic assumption made in the Bouguer–Lambert method. Similar to the exact values in Figure 6b and c, k generally decreased with size, but the trend was less significant under weak-absorption conditions. The k retrieved by the sphere models were close to those retrieved by the super-spheroid models. The differences were relatively higher under strong-absorption conditions and reached up to 0.0006, while they were less than

370 0.0001 under weak-absorption conditions. Therefore, retrieving the imaginary parts solely from the absorption coefficients was not sensitive to the model shape when the same size distributions were used.
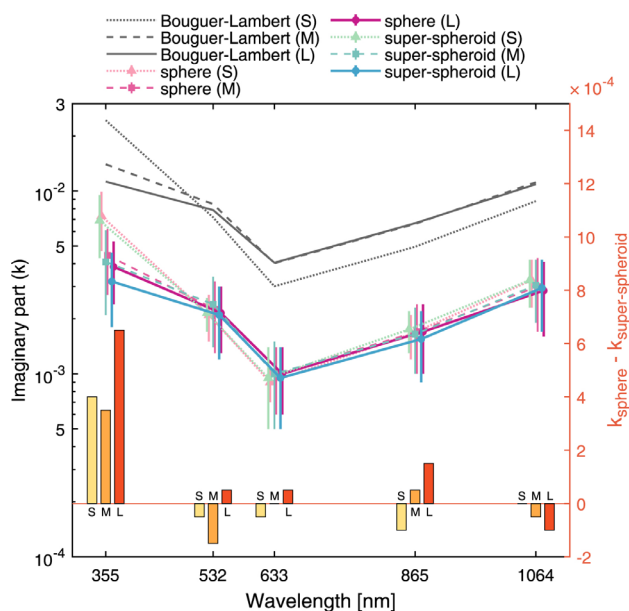

Figure 7: The wavelength-dependent imaginary parts (k) of refractive indices obtained from absorption coefficients (left y-axis) and the differences in k retrieved from the homogeneous sphere models and the homogeneous super-spheroid models (right y-axis)

375 **for different particle sizes (S, M, L) for E1/E2. The imaginary parts retrieved by the Bouguer–Lambert method are included for comparison. The error bar indicates half of the range of k, and the marker represents the mean of the range. To clarify the uncertainty of k, the data points are slightly shifted horizontally.**

Table 3: The refractive indices retrieved from the homogeneous sphere models and the homogeneous super-spheroid models at
380 **different sizes (S, M, L) at the wavelengths of 355 to 1064 nm for E1. "exact" indicates the exact refractive while "range" represents the range values as the measurement uncertainties are considered.**

Experiment			355 nm		532 nm		633 nm		865 nm		1064 nm	
E1			n	k	n	k	n	k	n	k	n	k
S	sphere	exact	1.44	0.0072	1.48	0.0021	1.49	0.0009	1.51	0.0016	1.52	0.0032
		range	1.40-1.53	0.0047-0.0099	1.45-1.51	0.0015-0.0027	1.47-1.51	0.0007-0.0011	1.49-1.53	0.0012-0.0021	1.50-1.53	0.0023-0.0042
	super-spheroid	exact	1.51	0.0070	1.50	0.0022	1.51	0.0008	1.52	0.0018	1.52	0.0033
		range	1.44-1.65	0.0043-0.0095	1.48-1.55	0.0017-0.0026	1.48-1.54	0.0005-0.0014	1.50-1.54	0.0013-0.0022	1.50-1.53	0.0023-0.0042
M	sphere	exact	nan	nan	nan	nan	nan	nan	1.59	0.0015	1.45	0.0032
		range	nan	0.0027-0.0062	nan	0.0013-0.0032	nan	0.0006-0.0014	1.40-1.70	0.0010-0.0024	1.40-1.70	0.0017-0.0043
	super-spheroid	exact	1.50	0.0039	1.53	0.0019	1.52	0.0010	1.54	0.0017	1.51	0.0031
		range	1.40-1.70	0.0021-0.0061	1.40-1.70	0.0014-0.0034	1.40-1.70	0.0005-0.0015	1.40-1.70	0.0010-0.0023	1.42-1.63	0.0019-0.0042
L	sphere	exact	nan	nan	nan	nan	nan	nan	nan	nan	nan	nan
		range	nan	0.0024-0.0053	nan	0.0013-0.0030	nan	0.0006-0.0014	nan	0.0010-0.0024	nan	0.0016-0.0041
	super-spheroid	exact	1.53	0.0030	1.52	0.0018	1.54	0.0010	1.48	0.0016	1.49	0.0029
		range	1.40-1.70	0.0018-0.0046	1.40-1.70	0.0012-0.0030	1.40-1.70	0.0005-0.0014	1.40-1.70	0.0009-0.0022	1.40-1.70	0.0017-0.0042

3.2 Retrieved refractive indices in E3/E4

Similar to Figure 5, the "measurements" and the look-up tables in E3 and E4 were illustrated in Figure 8. Note that a significant
385 discrepancy emerged between the "dust samples" and the homogeneous super-spheroid models as the size increased, which
was inconsistent with the findings in Figure 5. Furthermore, the discrepancy for the sphere models was even larger. This
discrepancy could be attributed to the differences in size distributions. These differences were not influenced by the size
descriptor of the non-spherical particle but were directly caused by the discrepancies in the optical properties between the "dust
samples" and the models when using the OPC to measure the size of individual particles. Therefore, it was difficult to
390 accurately retrieve n because the scattering coefficients were highly sensitive to the size distribution. However, retrieving k
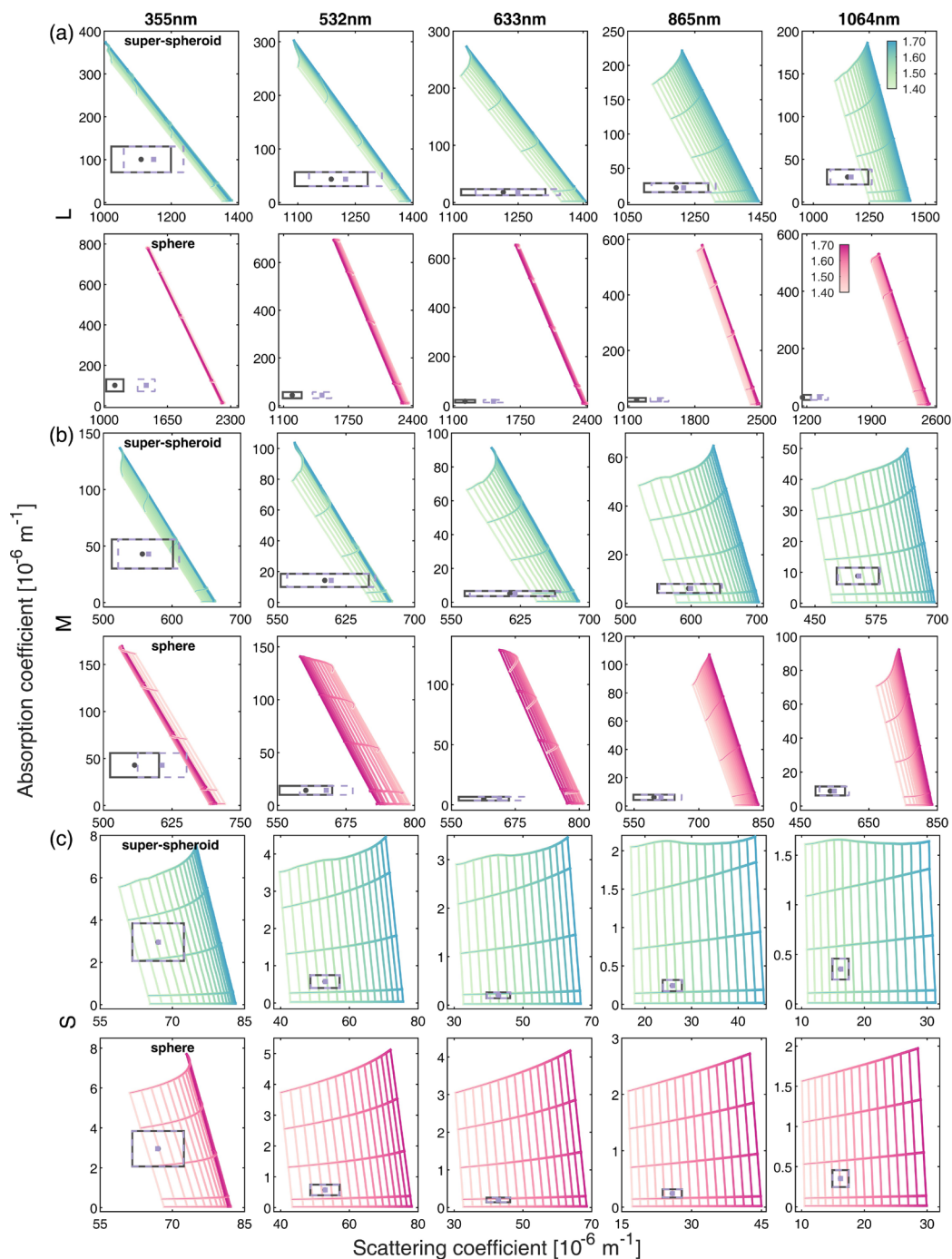from the absorption coefficients was still possible.

Figure 8: Results are similar to Figure 5, but represent for E3/E4.

395 In Figure 9a, the refractive indices retrieved by various models and methods in E3 are illustrated. Note that the differences in the refractive indices were insignificant between those obtained based on the sphere and super-spheroid models at small sizes. Additionally, in E3 and E4, the refractive indices retrieved from the Bouguer–Lambert method were model-dependent, which could be attributed to inconsistencies in the volume size distribution. The total volume of the dust particle ensemble was substantially smaller for the super-spheroid models compared to the sphere models (Figure 4), resulting in a higher absorptivity

400 of the medium. Consequently, the imaginary parts of the refractive indices were significantly higher for those using the super-spheroid models. Interestingly, the imaginary parts retrieved by the Bouguer–Lambert method using the sphere models (Figure 9a) were closer to the range values for the super-spheroid models (Figure 9b). In Figure 9b, the range values of k retrieved solely from the absorption coefficients for the sphere models were significantly smaller than the counterparts for the super-spheroid models at large sizes. The difference could range from approximately 0.002 in a high-absorption scenario (such as

405 355 nm) to as low as 0.0007 in a low-absorption scenario (such as 633 nm). However, the difference was insignificant at small sizes due to a relatively small discrepancy in the size distribution.

In comparing the refractive indices retrieved in E1 (Table 3) and E3 (Table 4), it is important to note that the range values of k retrieved using the super-spheroid models were generally consistent in both experiments. However, the values obtained using the sphere models were significantly smaller in E1 compared to E3, particularly at medium and large sizes. The accurate

410 retrieval of the real parts was only possible under very strict conditions in which there were no discrepancies in the size distribution and morphology between the "dust samples" and the models, specifically in E1. Despite this finding, the exact refractive indices could still be retrieved at small sizes. However, it should be noted that the refractive indices obtained at small sizes may not be applicable to large sizes as they depend on the sizes in the retrieval process when assuming a homogeneous model.
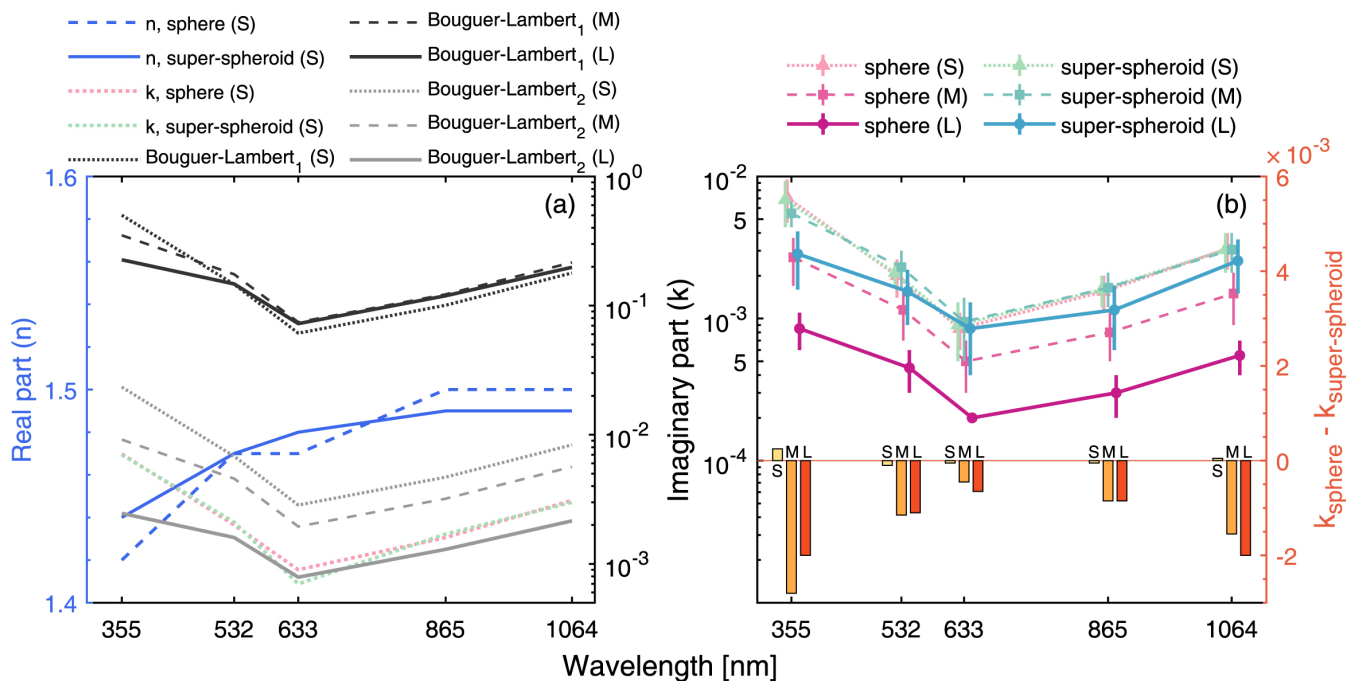
Figure 9: (a) The exact refractive indices retrieved from the homogeneous sphere models and the homogeneous super-spheroid models at small sizes (S) and the imaginary parts retrieved by the Bouguer–Lambert method for E3. Subscript 1 indicates that the volume of dust aerosols is calculated from the size distributions for the homogeneous super-spheroid models while the subscript 2 represents volume that for the homogeneous sphere models. **(b)** is similar to Figure 7, but represents for E3.

Table 4: Results are similar to those in Table 3, but represents for E3.

Experiment E3			355 nm		532 nm		633 nm		865 nm		1064nm	
			n	k	n	k	n	k	n	k	n	k
S	sphere	exact	1.42	0.0071	1.47	0.0020	1.47	0.0009	1.50	0.0016	1.50	0.0031
		range	1.40-1.48	0.0047-0.0095	1.44-1.49	0.0014-0.0026	1.46-1.50	0.0006-0.0011	1.48-1.52	0.0011-0.0020	1.48-1.52	0.0022-0.0040
	super-spheroid	exact	1.44	0.0070	1.47	0.0021	1.48	0.0007	1.49	0.0017	1.49	0.0030
		range	1.40-1.52	0.0044-0.0093	1.45-1.51	0.0017-0.0025	1.46-1.50	0.0005-0.0013	1.47-1.51	0.0012-0.0020	1.47-1.50	0.0021-0.0040
M	sphere	exact	nan	nan	nan	nan	nan	nan	nan	nan	nan	nan
		range	nan	0.0017-0.0037	nan	0.0007-0.0016	nan	0.0003-0.0007	nan	0.0005-0.0011	nan	0.0009-0.0021
	super-spheroid	exact	nan	nan	nan	nan	nan	nan	1.43	0.0018	1.45	0.0028
		range	nan	0.0044-0.0066	nan	0.0016-0.0030	nan	0.0005-0.0014	1.40-1.50	0.0012-0.0021	1.42-1.49	0.0021-0.0040
L	sphere	exact	nan	nan	nan	nan	nan	nan	nan	nan	nan	nan
		range	nan	0.0006-0.0011	nan	0.0003-0.0006	nan	0.0002-0.0002	nan	0.0002-0.0004	nan	0.0004-0.0007
	super-spheroid	exact	nan	nan	nan	nan	nan	nan	nan	nan	nan	nan
		range	nan	0.0016-0.0041	nan	0.0009-0.0022	nan	0.0004-0.0013	nan	0.0006-0.0017	nan	0.0015-0.0036

3.3 Comparison of the optical properties of "dust samples" with those calculated using the retrieved refractive indices

425 Compared to the fundamental microphysical properties, the variations in the calculated optical properties using different models are of greater concern in practical implementation. We compared the optical properties calculated from different models (sphere and super-spheroid) and different refractive indices, including the extinction coefficients (scattering coefficients + absorption coefficients), single scattering albedo (SSA), and asymmetry factor. The E4 scenario represented measurements closer to those obtained in the laboratory, while E1 was considered an ideal scenario. In most cases, the

430 discrepancies between the "measurement" and the look-up table were so significant that the scattering truncation correction could barely affect the retrieved refractive indices. The differences in optical properties between the results in E1 and E2, in addition to E3 and E4, were negligible. Thus, only the results from E1 and E3 are illustrated in Figure 10. Note that the real parts of the refractive indices could not be obtained in most cases in E1 and E3; hence, the real parts were set to 1.52 in such cases based on previous studies (Di Biagio et al., 2019; Dubovik et al., 2002; Müller et al., 2009; Wagner et al., 2012).
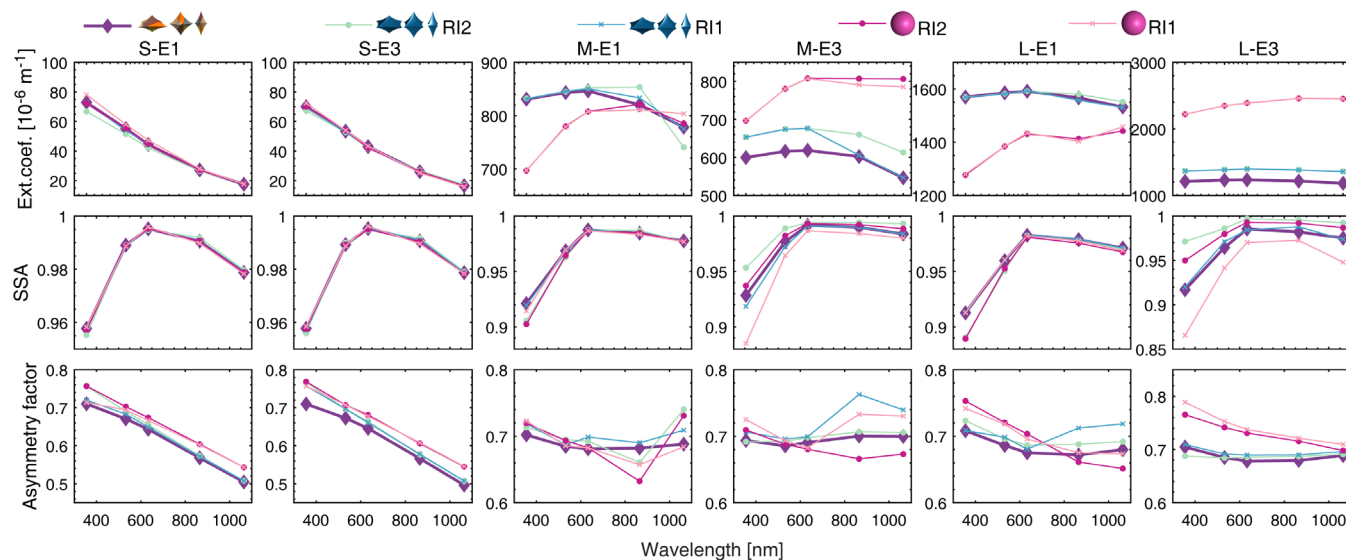
Figure 10: The optical properties of various models at different sizes for experiments E1 and E3. RI1 indicates that the refractive indices used for optical modelling are the retrieval results from the homogeneous super-spheroid models while RI2 means that those are from the homogeneous sphere models.

In E1, the size distributions were the same among various models, and no significant differences in the retrieved refractive indices between the super-spheroid and sphere models were found. However, when using the homogeneous super-spheroid models, the calculated optical properties were generally closer to the "measurements" compared to those using the sphere models in E1, emphasizing the importance of the model shape in simulating nonspherical dust aerosols. In E3, the differences in optical properties between the super-spheroid and sphere models were further amplified by the discrepancies in size distributions. These differences became more significant as the size increased.

The SSA was highly sensitive to the imaginary parts of the refractive indices. The SSA calculated using the super-spheroid model and the corresponding retrieved refractive indices showed good agreement with the "measurement" in E3. However, when using the sphere models, the results varied significantly from the "measurement" in M-E3 and L-E3.

In particular, the SSA for L-E3 shown in Figure 10 suggested that the imaginary parts retrieved from sphere models were underestimated. By utilizing the sphere model, the SSA calculated using the refractive indices retrieved from the sphere model was found to be larger than the "measurement", especially at large sizes. The underestimation in the imaginary parts of the sphere models resulted from significant discrepancies in the size distributions between the sphere model and the "dust sample". When assuming a spherical model, the OPC provided larger sizes than the "dust sample", which increased absorption coefficients of the model on a larger scale. As a result, the retrieved imaginary parts decreased.

The asymmetry factor was found to be more sensitive to the shape of models than the SSA, especially at large sizes. This finding was consistent with previous studies (Mishchenko et al., 1996; Otto et al., 2009). Generally, the sphere model showed a significant decreasing trend with wavelength and tended to overestimate the asymmetry factor, particularly at a relatively short wavelength (e.g., 355 nm). However, this decreasing trend was not evident at large sizes for the "dust sample". The

discrepancy in the asymmetry factor could introduce a significant bias in climate modelling, as many climate models utilized the sphere models (Balkanski et al., 2007; Hess et al., 1998; Hurrell et al., 2013; Mishchenko et al., 1995).

460 Significant variations were observed in the asymmetry factor at wavelengths of 865 nm and 1064 nm for M-E1 and M-E3 (Figure 10). These variations were attributed to the variations in the real parts of the refractive indices. To simply the discussion, the refractive indices retrieved from the homogeneous super-spheroid models were referred to as RI1, while those from the homogeneous sphere models were referred to as RI2. Below 865 nm, the real parts of RI2 were set to the default value of 1.52 for M-E1, and the same was done for RI1 for M-E3 as the "measurement" deviated significantly from the values

465 in the look-up table. However, at 865 nm and 1064 nm, the "measurement" fell within the look-up table, and the extinction coefficients were well matched in M-E1 and M-E3. Despite this, the retrieved real parts deviated significantly from the value of 1.52. Interestingly, the results implied that fixing the real parts to a value of 1.52 for all five selected wavelengths would be a better choice than using the retrieved values to reproduce the asymmetry factor of the "dust sample".

The significant variations in the asymmetry factor also indicated that, despite the good agreement in the scattering and

470 absorption coefficients between the measurements and the modelling, it did not guarantee accurate simulation of all the optical properties. For instance, reproducing the asymmetry factor calculated from the inhomogeneous models was challenging. This difficulty implied an inherent defect in homogeneous models, a finding that was also consistent with previous studies (Zong et al., 2021).

In Figure 11, the phase matrices of the "measurements" and those calculated based on the sphere and super-spheroid models

475 were illustrated. Note that the imaginary parts were large at small sizes, whereas they were small at large sizes. The trends in the phase matrices were mainly determined by the morphology of the particles. Significant discrepancies were observed between the results from the homogeneous sphere models and the "measurements". However, the results from the homogeneous super-spheroid models were in good agreement with the "measurements", especially in the low absorption scenario (i.e., L-E1 and L-E3). Nonetheless, the phase function (P_{11}) was less sensitive to the particle shape in the scenario of

480 high absorption (i.e., S-E1 and S-E3). Additionally, notable differences in the $-P_{12}/P_{11}$ and P_{22}/P_{11} were found between those calculated by the super-spheroid models using RI1 and RI2 for S-E1. These differences could be attributed to the variations in the real parts of the refractive indices. The optical properties in Figure 10 might imply that the differences between the homogeneous and inhomogeneous super-spheroid models were negligible at small sizes. However, Figure 11 indicated that significant discrepancies in the phase matrices still existed at small sizes, particularly in the backward direction.
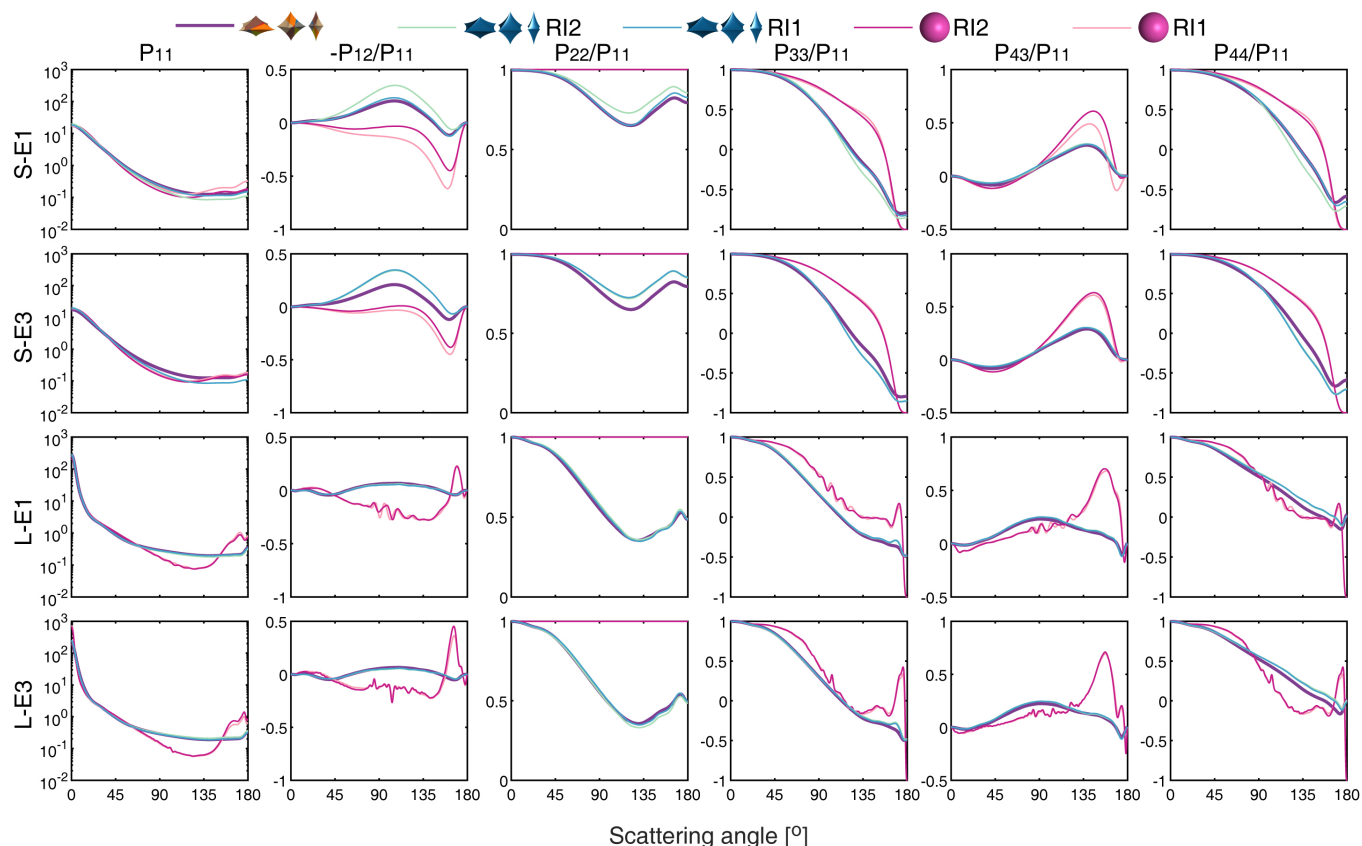
Figure 11: The phase matrices of various models at a wavelength of 355 nm and different sizes (S and L) for experiments E1 and E3.

3.4 Discussion about the actual laboratory scenario

It is not fair to quantitatively compare the refractive indices and the optical properties obtained in this study with those from actual laboratory measurements due to several assumptions made in the numerical experiments. For instance, we assumed that the refractive indices of various minerals were accurate. However, significant uncertainties in the refractive indices of hematite could be noted, and the refractive indices of goethite were only available for limited wavelengths and were based on a single study (Go et al., 2022). Besides, instrumental error was more complicated in the real world and discrepancies in size distribution between the model and the realistic particles existed. Nevertheless, the results in the numerical experiments provided a reference for investigating the extent to which the uncertainties resulting from the assumption of spherical particles could affect the actual laboratory measurements.

Previous studies have proven that the super-spheroid models with e=2.5 exhibited comparable non-sphericity to realistic dust aerosols (Kong et al., 2022; Lin et al., 2018, 2021). Therefore, it makes sense to believe that the super-spheroid models should produce similar results for the size correction, the scattering truncation correction, and the optical properties as the actual particles. The size distribution in actual laboratory measurements for the dust sample from Algeria conducted by Di Biagio et

500   al. (2019) is the same as the size distribution for size L in E3/E4. Thus, the results in L-E3 are the most representative of the results in actual laboratory measurements.

As discussed in Sect. 3.3, the sphere models tended to overestimate the asymmetry factor and the SSA. The k obtained by Di Biagio et al. (2019) lay between the results obtained from the homogeneous sphere models and the homogeneous super-spheroid models in E3/E4, indicating that the uncertainties resulting from the discrepancies in morphology between the sphere

505   model and realistic particles in actual laboratory measurements might be smaller than those in the numerical experiments. Quantitatively, for the actual laboratory measurements, such uncertainties in k and SSA should be smaller than 0.002 and 0.03, respectively, under conditions of high absorption. Under weak-absorption conditions, the uncertainties should be smaller than 0.0007 and 0.01, respectively (see Figure 9 and 10). It was difficult to obtain accurate values of the real parts of the refractive indices from the scattering coefficients due to the discrepancies in morphology and size distributions between the models and

510   the actual particles. Thus, the real parts might be obtained by some other methods or simply set to a representative value (Grams et al., 1974; Patterson et al., 1977; Sokolik et al., 1993). The uncertainty in the asymmetry factor was significant, which could reach up to 0.04 at relatively short wavelengths. However, these quantitative values might be further amplified by the presence of exceptionally large particles in the atmosphere (Adebiyi et al., 2023a), which were not considered in this study. The phase matrices were primarily influenced by the shape of the model and were more sensitive to the real parts than the

515   imaginary parts. Considering a specific model, the uncertainties in the phase matrices resulting from the refractive indices obtained using different models were acceptable.

4 Summary

Dust aerosols are rarely homogeneous and spherical. However, when measuring their refractive indices in the laboratory, it is often assumed that the particles are homogeneous and spherical. In this study, we conducted a theoretical investigation to

520   explore the uncertainties associated with laboratory measurements of refractive indices for dust aerosols in the wavelength range of 355 to 1064 nm. Additionally, we aimed to determine the impact of these uncertainties on the optical properties of dust aerosols. This is a crucial step in validating the fundamental microphysical properties of dust aerosols and understanding the extent of uncertainties before applying them in specific research.

Four numerical experiments were conducted to study the uncertainties in different scenarios, taking into account size correction

525   and scattering truncation correction due to instrumental bias in OPC and nephelometer. In these numerical experiments, dust samples were considered as the inhomogeneous super-spheroid models, and the corresponding optical properties were treated as the measurements. Homogeneous super-spheroid models and homogeneous sphere models were used to retrieve refractive indices. Two methods, the look-up table and the Bouguer–Lambert method, were used for comparison. Additionally, the refractive indices obtained at different sizes (small, medium, and large) were also examined.

530   Under an ideal scenario, where no instrumental defects needed to be corrected, the look-up tables for the homogeneous super-spheroid models were able to fit the measurements at any size. However, the look-up tables for the sphere models were only

suitable for small sizes due to significant discrepancies in the scattering coefficients at larger sizes. Nevertheless, the imaginary parts of the refractive indices could be obtained solely from the absorption coefficients. The differences in the imaginary parts obtained from the super-spheroid and sphere models were insignificant, with a maximum value of 0.0006 observed under high-absorption conditions.

Under a more realistic scenario, in which the size correction and the scattering truncation corrections were applied, the refractive indices could be retrieved from the look-up tables by using both the super-spheroid and sphere models at a small size. The differences in refractive indices resulting from morphology were insignificant at a small size, similar to those under the ideal scenario. However, neither the look-up tables for the super-spheroid models nor the sphere models could account for the measurements at larger sizes because of the differences in size distributions between the "dust samples" and the models. This finding suggests that accurate refractive indices can only be obtained under ideal conditions in which no discrepancies in morphology and size distribution between the "dust samples" and models exist.

Although accurately retrieving both the real parts and the imaginary parts of the refractive indices could be challenging, it was still possible to retrieve the imaginary parts solely from the absorption coefficients. The imaginary parts retrieved for the sphere models were significantly smaller than those for the super-spheroid models. The differences could reach up to approximately 0.002 under high absorption conditions and be smaller than 0.0007 under weak-absorption conditions. In all experiments, the imaginary parts retrieved using the Bouguer–Lambert method were higher than those obtained from the look-up tables. However, in a more realistic scenario, the imaginary parts retrieved using the Bouguer-Lambert method and sphere models were happened to be closer to the results from the look-up tables due to the discrepancy in size distribution. As for the real parts, they could be obtained through alternative methods or simply set to a representative value (Grams et al., 1974; Patterson et al., 1977; Sokolik et al., 1993). The value of 1.52 was found to be suitable for the real parts at the short wavelengths.

The retrieved refractive indices were found to be size-dependent. As the size increased, the imaginary parts decreased. Even though the refractive indices could be retrieved at small sizes, they could not be used for large particles. The size-dependent refractive indices resulted from the inherent defects in the homogeneous models used to characterize the inhomogeneous particles.

Based on the retrieved refractive indices, the corresponding optical properties were compared with the true values. If the refractive indices could not be retrieved, the real parts were set to 1.52 based on previous studies (Di Biagio et al., 2019; Dubovik et al., 2002; Müller et al., 2009; Wagner et al., 2012). Generally, the sphere models tended to overestimate the asymmetry factor and the SSA, while the super-spheroid models were in good agreement with the true values. Such overestimation could result in significant biases in climate modelling, as many climate models also utilized sphere models (Balkanski et al., 2007; Hess et al., 1998; Hurrell et al., 2013; Mishchenko et al., 1995). Therefore, we recommend using nonspherical models, such as the super-spheroid model, for retrieving the refractive indices of dust aerosols and climate modelling.

The uncertainties arising from assuming spherical particles in the numerical experiments were believed to be comparable to those based on actual laboratory measurements. Under conditions of high absorption, the uncertainties in k and SSA should

be smaller than 0.002 and 0.03, respectively. Conversely, under conditions of weak absorption, the uncertainties should be smaller than 0.0007 and 0.01, respectively. Additionally, the uncertainty in the asymmetry factor may reach up to 0.04 or even larger, as it is highly sensitive to the real parts of the refractive indices and size distributions. These quantitative values might be further amplified due to the presence of unexceptionally coarse particles that were not considered in this study (Adebiyi et

570   al., 2023a). The phase matrices were primarily influenced by morphology. Not surprisingly, the uncertainties in the phase matrices resulting from the refractive indices that were retrieved using different models were generally acceptable within a specific model.

The findings of this study provide valuable insights into the uncertainties associated with currently available laboratory-measured refractive indices (Di Biagio et al., 2019). It is important to note that the optical properties of inhomogeneous

575   particles cannot be fully characterized based on homogeneous models. However, there is still a long way to go in developing a comprehensive and suitable database of inhomogeneous dust models that can be applied in various fields such as remote sensing and climate models (Wang et al., 2022). Previously, homogeneous models were the only option, but the ultimate goal is to accurately characterize realistic dust aerosols using inhomogeneous models. Further efforts to improve the computational efficiency are crucial for calculating the optical properties of nonspherical particles with large size parameters. The use of

580   GPU-accelerated computing and data-driven techniques shows promise in this regard (Bi et al., 2022; Yu et al., 2022). Additionally, future work should focus on studying the refractive indices of individual minerals, as well as the mineral composition and internal structure of dust aerosols, rather than solely focusing on the refractive indices of entire dust particles.

Data availability

585 The data used in the numerical experiments are available at (will be updated when ready to publish).

Author contribution

SK and LB designed the experiments and SK carried them out. ZW developed the code for calculating the optical properties of inhomogeneous models. SK prepared the manuscript with contributions from all co-authors. LB revised the manuscript.

Competing interests

590 The authors declare that they have no conflict of interest.

Acknowledgements

References

Ackerman, A. S., Toon, O. B., Stevens, D. E., Heymsfield, A. J., Ramanathan, V., and Welton, E. J.: Reduction of Tropical Cloudiness by Soot, Science, 288, 1042–1047, https://doi.org/10.1126/science.288.5468.1042, 2000.

Adebiyi, A., Kok, J. F., Murray, B. J., Ryder, C. L., Stuut, J.-B. W., Kahn, R. A., Knippertz, P., Formenti, P., Mahowald, N.
600 M., Pérez García-Pando, C., Klose, M., Ansmann, A., Samset, B. H., Ito, A., Balkanski, Y., Di Biagio, C., Romanias, M. N., Huang, Y., and Meng, J.: A review of coarse mineral dust in the Earth system, Aeolian Res., 60, 100849, https://doi.org/10.1016/j.aeolia.2022.100849, 2023a.

Adebiyi, A. A., Huang, Y., Samset, B. H., and Kok, J. F.: Observations suggest that North African dust absorbs less solar radiation than models estimate, Commun. Earth Environ., 4, 1–13, https://doi.org/10.1038/s43247-023-00825-2, 2023b.

605 Arnott, W. P., Hamasha, K., Moosmüller, H., Sheridan, P. J., and Ogren, J. A.: Towards Aerosol Light-Absorption Measurements with a 7-Wavelength Aethalometer: Evaluation with a Photoacoustic Instrument and 3-Wavelength Nephelometer, Aerosol Sci. Technol., 39, 17–29, https://doi.org/10.1080/027868290901972, 2005.

Atkinson, J. D., Murray, B. J., Woodhouse, M. T., Whale, T. F., Baustian, K. J., Carslaw, K. S., Dobbie, S., O'Sullivan, D., and Malkin, T. L.: The importance of feldspar for ice nucleation by mineral dust in mixed-phase clouds, Nature, 498, 355–
610 358, https://doi.org/10.1038/nature12278, 2013.

Balkanski, Y., Schulz, M., Claquin, T., and Guibert, S.: Reevaluation of Mineral aerosol radiative forcings suggests a better agreement with satellite and AERONET data, Atmospheric Chem. Phys., 7, 81–95, https://doi.org/10.5194/acp-7-81-2007, 2007.

Bedidi, A. and Cervelle, B.: Light scattering by spherical particles with hematite and goethitelike optical properties: Effect of

615   water impregnation, J. Geophys. Res. Solid Earth, 98, 11941–11952, https://doi.org/10.1029/93JB00188, 1993.

Bi, L. and Yang, P.: Accurate simulation of the optical properties of atmospheric ice crystals with the invariant imbedding T-matrix method, J. Quant. Spectrosc. Radiat. Transf., 138, 17–35, https://doi.org/10.1016/j.jqsrt.2014.01.013, 2014.

Bi, L. and Yang, P.: Improved ice particle optical property simulations in the ultraviolet to far-infrared regime, J. Quant. Spectrosc. Radiat. Transf., 189, 228–237, https://doi.org/10.1016/j.jqsrt.2016.12.007, 2017.

620   Bi, L., Yang, P., Kattawar, G. W., and Kahn, R.: Single-scattering properties of triaxial ellipsoidal particles for a size parameter range from the Rayleigh to geometric-optics regimes, Appl. Opt., 48, 114–126, https://doi.org/10.1364/AO.48.000114, 2009.

Bi, L., Yang, P., Kattawar, G. W., and Kahn, R.: Modeling optical properties of mineral aerosol particles by using nonsymmetric hexahedra, Appl. Opt., 49, 334–342, https://doi.org/10.1364/AO.49.000334, 2010.

Bi, L., Yang, P., Kattawar, G. W., and Mishchenko, M. I.: Efficient implementation of the invariant imbedding T-matrix

625   method and the separation of variables method applied to large nonspherical inhomogeneous particles, J. Quant. Spectrosc. Radiat. Transf., 116, 169–183, https://doi.org/10.1016/j.jqsrt.2012.11.014, 2013.

Bi, L., Lin, W., Liu, D., and Zhang, K.: Assessing the depolarization capabilities of nonspherical particles in a super-ellipsoidal shape space, Opt. Express, 26, 1726–1742, https://doi.org/10.1364/OE.26.001726, 2018a.

Bi, L., Lin, W., Wang, Z., Tang, X., Zhang, X., and Yi, B.: Optical Modeling of Sea Salt Aerosols: The Effects of Nonsphericity

630   and Inhomogeneity, J. Geophys. Res. Atmospheres, 123, 543–558, https://doi.org/10.1002/2017jd027869, 2018b.

Bi, L., Wang, Z., Han, W., Li, W., and Zhang, X.: Computation of Optical Properties of Core-Shell Super-Spheroids Using a GPU Implementation of the Invariant Imbedding T-Matrix Method, Front. Remote Sens., 3, https://doi.org/10.3389/frsen.2022.903312, 2022.

Bohren, C. F. and Huffman, D. R.: Absorption and Scattering of Light by Small Particles, John Wiley & Sons, New York, 547

635   pp., 2008.

Bundke, U., Berg, M., Houben, N., Ibrahim, A., Fiebig, M., Tettich, F., Klaus, C., Franke, H., and Petzold, A.: The IAGOS-CORE aerosol package: instrument design, operation and performance for continuous measurement aboard in-service aircraft, 67, 28339, https://doi.org/10.3402/tellusb.v67.28339, 2015.

Chen, G., Ziemba, L. D., Chu, D. A., Thornhill, K. L., Schuster, G. L., Winstead, E. L., Diskin, G. S., Ferrare, R. A., Burton,

640   S. P., Ismail, S., Kooi, S. A., Omar, A. H., Slusher, D. L., Kleb, M. M., Reid, J. S., Twohy, C. H., Zhang, H., and Anderson, B. E.: Observations of Saharan dust microphysical and optical properties from the Eastern Atlantic during NAMMA airborne field campaign, Atmospheric Chem. Phys., 11, 723–740, https://doi.org/10.5194/acp-11-723-2011, 2011.

Collaud Coen, M., Weingartner, E., Apituley, A., Ceburnis, D., Fierz-Schmidhauser, R., Flentje, H., Henzing, J. S., Jennings, S. G., Moerman, M., Petzold, A., Schmid, O., and Baltensperger, U.: Minimizing light absorption measurement artifacts of the

645 Aethalometer: evaluation of five correction algorithms, Atmospheric Meas. Tech., 3, 457–474, https://doi.org/10.5194/amt-3-457-2010, 2010.

Di Biagio, C., Formenti, P., Cazaunau, M., Pangui, E., Marchand, N., and Doussin, J.-F.: Aethalometer multiple scattering correction C_{ref} for mineral dust aerosols, Atmospheric Meas. Tech., 10, 2923–2939, https://doi.org/10.5194/amt-10-2923-2017, 2017a.

650 Di Biagio, C., Formenti, P., Balkanski, Y., Caponi, L., Cazaunau, M., Pangui, E., Journet, E., Nowak, S., Caquineau, S., Andreae, M. O., Kandler, K., Saeed, T., Piketh, S., Seibert, D., Williams, E., and Doussin, J.-F.: Global scale variability of the mineral dust long-wave refractive index: a new dataset of in situ measurements for climate modeling and remote sensing, Atmospheric Chem. Phys., 17, 1901–1929, https://doi.org/10.5194/acp-17-1901-2017, 2017b.

Di Biagio, C., Formenti, P., Balkanski, Y., Caponi, L., Cazaunau, M., Pangui, E., Journet, E., Nowak, S., Andreae, M. O., 655 Kandler, K., Saeed, T., Piketh, S., Seibert, D., Williams, E., and Doussin, J.-F.: Complex refractive indices and single-scattering albedo of global dust aerosols in the shortwave spectrum and relationship to size and iron content, Atmospheric Chem. Phys., 19, 15503–15531, https://doi.org/10.5194/acp-19-15503-2019, 2019.

Di Biagio, C., Balkanski, Y., Albani, S., Boucher, O., and Formenti, P.: Direct Radiative Effect by Mineral Dust Aerosols Constrained by New Microphysical and Spectral Optical Data, Geophys. Res. Lett., 47, e2019GL086186, 660 https://doi.org/10.1029/2019GL086186, 2020.

Dubovik, O., Smirnov, A., Holben, B. N., King, M. D., Kaufman, Y. J., Eck, T. F., and Slutsker, I.: Accuracy assessments of aerosol optical properties retrieved from Aerosol Robotic Network (AERONET) Sun and sky radiance measurements, J. Geophys. Res. Atmospheres, 105, 9791–9806, https://doi.org/10.1029/2000JD900040, 2000.

Dubovik, O., Holben, B., Eck, T. F., Smirnov, A., Kaufman, Y. J., King, M. D., Tanré, D., and Slutsker, I.: Variability of 665 Absorption and Optical Properties of Key Aerosol Types Observed in Worldwide Locations, J. Atmospheric Sci., 59, 590–608, https://doi.org/10.1175/1520-0469(2002)059<0590:VOAAOP>2.0.CO;2, 2002.

Dubovik, O., Sinyuk, A., Lapyonok, T., Holben, B. N., Mishchenko, M., Yang, P., Eck, T. F., Volten, H., Muñoz, O., Veihelmann, B., Zande, W. J. van der, Leon, J.-F., Sorokin, M., and Slutsker, I.: Application of spheroid models to account for aerosol particle nonsphericity in remote sensing of desert dust, J. Geophys. Res. Atmospheres, 111, 670 https://doi.org/10.1029/2005jd006619, 2006.

Egan, W. G. and Hilgeman, T. W.: CHAPTER V - OPTICAL COMPLEX INDEX OF REFRACTION BETWEEN 0.185 AND 2.6 μm, in: Optical Properties of Inhomogeneous Materials, edited by: Egan, W. G. and Hilgeman, T. W., Academic Press, 73–125, https://doi.org/10.1016/B978-0-12-232650-9.50009-6, 1979.

Go, S., Lyapustin, A., Schuster, G. L., Choi, M., Ginoux, P., Chin, M., Kalashnikova, O., Dubovik, O., Kim, J., da Silva, A., 675 Holben, B., and Reid, J. S.: Inferring iron-oxide species content in atmospheric mineral dust from DSCOVR EPIC observations, Atmospheric Chem. Phys., 22, 1395–1423, https://doi.org/10.5194/acp-22-1395-2022, 2022.

Grams, G. W., Blifford, I. H., Gillette, D. A., and Russell, P. B.: Complex Index of Refraction of Airborne Soil Particles, J. Appl. Meteorol. Climatol., 13, 459–471, https://doi.org/10.1175/1520-0450(1974)013<0459:CIOROA>2.0.CO;2, 1974.

Hansen, A. D. A., Rosen, H., and Novakov, T.: The aethalometer — An instrument for the real-time measurement of optical

680   absorption by aerosol particles, Sci. Total Environ., 36, 191–196, https://doi.org/10.1016/0048-9697(84)90265-1, 1984.

Hansen, J., Sato, M., and Ruedy, R.: Radiative forcing and climate response, J. Geophys. Res. Atmospheres, 102, 6831–6864, https://doi.org/10.1029/96JD03436, 1997.

Heim, M., Mullins, B. J., Umhauer, H., and Kasper, G.: Performance evaluation of three optical particle counters with an efficient "multimodal" calibration method, J. Aerosol Sci., 39, 1019–1031, https://doi.org/10.1016/j.jaerosci.2008.07.006,

685   2008.

Hess, M., Koepke, P., and Schult, I.: Optical Properties of Aerosols and Clouds: The Software Package OPAC, Bull. Am. Meteorol. Soc., 79, 14, https://doi.org/10.1175/1520-0477(1998)079<0831:OPOAAC>2.0.CO;2, 1998.

Huang, Y., Adebiyi, A. A., Formenti, P., and Kok, J. F.: Linking the Different Diameter Types of Aspherical Desert Dust Indicates That Models Underestimate Coarse Dust Emission, Geophys. Res. Lett., 48, e2020GL092054,

690   https://doi.org/10.1029/2020GL092054, 2021.

Hurrell, J. W., Holland, M. M., Gent, P. R., Ghan, S., Kay, J. E., Kushner, P. J., Lamarque, J.-F., Large, W. G., Lawrence, D., Lindsay, K., Lipscomb, W. H., Long, M. C., Mahowald, N., Marsh, D. R., Neale, R. B., Rasch, P., Vavrus, S., Vertenstein, M., Bader, D., Collins, W. D., Hack, J. J., Kiehl, J., and Marshall, S.: The Community Earth System Model: A Framework for Collaborative Research, Bull. Am. Meteorol. Soc., 94, 1339–1360, https://doi.org/10.1175/BAMS-D-12-00121.1, 2013.

695   Jeong, G. Y.: Mineralogy and geochemistry of Asian dust: dependence on migration path, fractionation, and reactions with polluted air, Atmospheric Chem. Phys., 20, 7411–7428, https://doi.org/10.5194/acp-20-7411-2020, 2020.

Jeong, G. Y. and Nousiainen, T.: TEM analysis of the internal structures and mineralogy of Asian dust particles and the implications for optical modeling, Atmospheric Chem. Phys., 14, 7233–7254, https://doi.org/10.5194/acp-14-7233-2014, 2014.

700   Kahnert, M.: Modelling radiometric properties of inhomogeneous mineral dust particles: Applicability and limitations of effective medium theories, J. Quant. Spectrosc. Radiat. Transf., 152, 16–27, https://doi.org/10.1016/j.jqsrt.2014.10.025, 2015.

Kalashnikova, O. V. and Sokolik, I. N.: Modeling the radiative properties of nonspherical soil-derived mineral aerosols, J. Quant. Spectrosc. Radiat. Transf., 87, 137–166, https://doi.org/10.1016/j.jqsrt.2003.12.026, 2004.

Kandler, K., Benker, N., Bundke, U., Cuevas, E., Ebert, M., Knippertz, P., Rodríguez, S., Schütz, L., and Weinbruch, S.:

705   Chemical composition and complex refractive index of Saharan Mineral Dust at Izaña, Tenerife (Spain) derived by electron microscopy, Atmos. Environ., 41, 8058–8074, https://doi.org/10.1016/j.atmosenv.2007.06.047, 2007.

Kandler, K., Schütz, L., Deutscher, C., Ebert, M., Hofmann, H., Jäckel, S., Jaenicke, R., Knippertz, P., Lieke, K., Massling, A., Petzold, A., Schladitz, A., Weinzierl, B., Wiedensohler, A., Zorn, S., and Weinbruch1, S.: Size distribution, mass concentration, chemical and mineralogical composition and derived optical parameters of the boundary layer aerosol at Tinfou,

710   Morocco, during SAMUM 2006, Tellus B Chem. Phys. Meteorol., 61, 32–50, https://doi.org/10.1111/j.1600-0889.2008.00385.x, 2009.

Kemppinen, O., Nousiainen, T., and Jeong, G. Y.: Effects of dust particle internal structure on light scattering, Atmospheric Chem. Phys., 15, 12011–12027, https://doi.org/10.5194/acp-15-12011-2015, 2015a.

Kemppinen, O., Nousiainen, T., Merikallio, S., and Räisänen, P.: Retrieving microphysical properties of dust-like particles using ellipsoids: the case of refractive index, Atmospheric Chem. Phys., 15, 11117–11132, https://doi.org/10.5194/acp-15-11117-2015, 2015b.

Khashan, M. A. and Nassif, A. Y.: Dispersion of the optical constants of quartz and polymethyl methacrylate glasses in a wide spectral range: 0.2–3 μm, Opt. Commun., 188, 129–139, https://doi.org/10.1016/S0030-4018(00)01152-4, 2001.

Kinne, S., Schulz, M., Textor, C., Guibert, S., Balkanski, Y., Bauer, S. E., Berntsen, T., Berglen, T. F., Boucher, O., Chin, M., Collins, W., Dentener, F., Diehl, T., Easter, R., Feichter, J., Fillmore, D., Ghan, S., Ginoux, P., Gong, S., Grini, A., Hendricks, J., Herzog, M., Horowitz, L., Isaksen, I., Iversen, T., Kirkevåg, A., Kloster, S., Koch, D., Kristjansson, J. E., Krol, M., Lauer, A., Lamarque, J. F., Lesins, G., Liu, X., Lohmann, U., Montanaro, V., Myhre, G., Penner, J., Pitari, G., Reddy, S., Seland, O., Stier, P., Takemura, T., and Tie, X.: An AeroCom initial assessment – optical properties in aerosol component modules of global models, Atmospheric Chem. Phys., 6, 1815–1834, https://doi.org/10.5194/acp-6-1815-2006, 2006.

Kok, J. F., Storelvmo, T., Karydis, V. A., Adebiyi, A. A., Mahowald, N. M., Evan, A. T., He, C., and Leung, D. M.: Mineral dust aerosol impacts on global climate and climate change, Nat. Rev. Earth Environ., 4, 71–86, https://doi.org/10.1038/s43017-022-00379-5, 2023.

Kong, S., Sato, K., and Bi, L.: Lidar Ratio–Depolarization Ratio Relations of Atmospheric Dust Aerosols: The Super-Spheroid Model and High Spectral Resolution Lidar Observations, J. Geophys. Res. Atmospheres, 127, e2021JD035629, https://doi.org/10.1029/2021JD035629, 2022.

Lee, K.-M., Choi, H., and Kim, J.: Refractive Index for Asian Dust in the Ultraviolet-Visible Region Determined From Compositional Analysis and Validated With OMI Observations, J. Geophys. Res. Atmospheres, 125, e2019JD030629, https://doi.org/10.1029/2019JD030629, 2020.

Li, M., Bi, L., Lin, W., Weng, F., He, S., and Zhang, X.: The Inhomogeneity Effect of Sea Salt Aerosols on the TOA Polarized Radiance at the Scattering Angles Ranging From 170° to 175°, IEEE Trans. Geosci. Remote Sens., 60, 1–12, https://doi.org/10.1109/TGRS.2021.3099026, 2022.

Lin, W., Bi, L., and Dubovik, O.: Assessing Superspheroids in Modeling the Scattering Matrices of Dust Aerosols, J. Geophys. Res. Atmospheres, 123, 13917–13943, https://doi.org/10.1029/2018jd029464, 2018.

Lin, W., Bi, L., Weng, F., Li, Z., and Dubovik, O.: Capability of Superspheroids for Modeling PARASOL Observations Under Dusty-Sky Conditions, J. Geophys. Res. Atmospheres, 126, e2020JD033310, https://doi.org/10.1029/2020jd033310, 2021.

Lindqvist, H., Jokinen, O., Kandler, K., Scheuvens, D., and Nousiainen, T.: Single scattering by realistic, inhomogeneous mineral dust particles with stereogrammetric shapes, Atmospheric Chem. Phys., 14, 143–157, https://doi.org/10.5194/acp-14-143-2014, 2014.

Longtin, D. R., Shettle, E. P., Hummel, J. R., and Pryce, J. D.: A Wind Dependent Desert Aerosol Model: Radiative Properties, OptiMetrics Inc, Burlington, Massachusetts, 1988.

McConnell, C. L., Formenti, P., Highwood, E. J., and Harrison, M. a. J.: Using aircraft measurements to determine the refractive index of Saharan dust during the DODO Experiments, Atmospheric Chem. Phys., 10, 3081–3098, https://doi.org/10.5194/acp-10-3081-2010, 2010.

750   Mishchenko, M. I., Lacis, A. A., Carlson, B. E., and Travis, L. D.: Nonsphericity of dust-like tropospheric aerosols: Implications for aerosol remote sensing and climate modeling, Geophys. Res. Lett., 22, 1077–1080, https://doi.org/10.1029/95GL00798, 1995.

Mishchenko, M. I., Travis, L. D., and Mackowski, D. W.: T-matrix computations of light scattering by nonspherical particles: A review, J. Quant. Spectrosc. Radiat. Transf., 55, 535–575, https://doi.org/10.1016/0022-4073(96)00002-7, 1996.

Mishchenko, M. I., Travis, L. D., Kahn, R. A., and West, R. A.: Modeling phase functions for dustlike tropospheric aerosols 755   using a shape mixture of randomly oriented polydisperse spheroids, J. Geophys. Res. Atmospheres, 102, 16831–16847, https://doi.org/10.1029/96JD02110, 1997.

Mishchenko, M. I., Hovenier, J. W., and Travis, L. D. (Eds.): Light Scattering by Nonspherical Particles: Theory, Measurements, and Applications, Academic Press, San Diego, 2000.

Müller, T., Schladitz, A., Massling, A., Kaaden, N., Kandler, K., and Wiedensohler, A.: Spectral absorption coefficients and 760   imaginary parts of refractive indices of Saharan dust during SAMUM-1, Tellus B Chem. Phys. Meteorol., 61, 79–95, https://doi.org/10.1111/j.1600-0889.2008.00399.x, 2009.

Müller, T., Schladitz, A., Kandler, K., and Wiedensohler, A.: Spectral particle absorption coefficients, single scattering albedos and imaginary parts of refractive indices from ground based in situ measurements at Cape Verde Island during SAMUM-2, Tellus B Chem. Phys. Meteorol., 63, 573–588, https://doi.org/10.1111/j.1600-0889.2011.00572.x, 2011.

765   Orofino, V., Blanco, A., Fonti, S., Proce, R., and Rotundi, A.: The infrared optical constants of limestone particles and implications for the search of carbonates on Mars, Planet. Space Sci., 46, 1659–1669, https://doi.org/10.1016/S0032-0633(98)00046-4, 1998.

Otto, S., Bierwirth, E., Weinzierl, B., Kandler, K., Esselborn, M., Tesche, M., Schladitz, A., Wendisch, M., and Trautmann, T.: Solar radiative effects of a Saharan dust plume observed during SAMUM assuming spheroidal model particles, Tellus B, 770   61, 270–296, https://doi.org/10.1111/j.1600-0889.2008.00389.x, 2009.

Patterson, E. M., Gillette, D. A., and Stockton, B. H.: Complex index of refraction between 300 and 700 nm for Saharan aerosols, J. Geophys. Res. 1896-1977, 82, 3153–3160, https://doi.org/10.1029/jc082i021p03153, 1977.

Petzold, A., Rasp, K., Weinzierl, B., Esselborn, M., Hamburger, T., Döckrnbrack, A., Kandler, K., Schütz, L., Knippertz, P., Fiebig, M., and Virkkula, A.: Saharan dust absorption and refractive index from aircraft-based observations during SAMUM 775   2006, Tellus B Chem. Phys. Meteorol., 61, 118–130, https://doi.org/10.1111/j.1600-0889.2008.00383.x, 2009.

Querry, M. R.: Optical Constants of Minerals and Other Materials from the Millimeter to the Ultraviolet, Chemical Research, Development & Engineering Center, U.S. Army Armament Munitions Chemical Command, 329 pp., 1987.

Reid, J. S., Jonsson, H. H., Maring, H. B., Smirnov, A., Savoie, D. L., Cliff, S. S., Reid, E. A., Livingston, J. M., Meier, M. M., Dubovik, O., and Tsay, S.-C.: Comparison of size and morphological measurements of coarse mode dust particles from Africa, J. Geophys. Res. Atmospheres, 108, https://doi.org/10.1029/2002jd002485, 2003.

Rocha-Lima, A., Martins, J. V., Remer, L. A., Todd, M., Marsham, J. H., Engelstaedter, S., Ryder, C. L., Cavazos-Guerra, C., Artaxo, P., Colarco, P., and Washington, R.: A detailed characterization of the Saharan dust collected during the Fennec campaign in 2011: in situ ground-based and laboratory measurements, Atmospheric Chem. Phys., 18, 1023–1043, https://doi.org/10.5194/acp-18-1023-2018, 2018.

Roush, T. L.: Estimation of visible, near-, and mid-infrared complex refractive indices of calcite, dolomite, and magnesite, Icarus, 354, 114056, https://doi.org/10.1016/j.icarus.2020.114056, 2021.

Ryder, C. L., Highwood, E. J., Rosenberg, P. D., Trembath, J., Brooke, J. K., Bart, M., Dean, A., Crosier, J., Dorsey, J., Brindley, H., Banks, J., Marsham, J. H., McQuaid, J. B., Sodemann, H., and Washington, R.: Optical properties of Saharan dust aerosol and contribution from the coarse mode as measured during the Fennec 2011 aircraft campaign, Atmospheric Chem. Phys., 13, 303–325, https://doi.org/10.5194/acp-13-303-2013, 2013.

Ryder, C. L., Marenco, F., Brooke, J. K., Estelles, V., Cotton, R., Formenti, P., McQuaid, J. B., Price, H. C., Liu, D., Ausset, P., Rosenberg, P. D., Taylor, J. W., Choularton, T., Bower, K., Coe, H., Gallagher, M., Crosier, J., Lloyd, G., Highwood, E. J., and Murray, B. J.: Coarse-mode mineral dust size distributions, composition and optical properties from AER-D aircraft measurements over the tropical eastern Atlantic, Atmospheric Chem. Phys., 18, 17225–17257, https://doi.org/10.5194/acp-18-17225-2018, 2018.

Saito, M. and Yang, P.: Generalization of Atmospheric Nonspherical Particle Size: Interconversions of Size Distributions and Optical Equivalence, J. Atmospheric Sci., 79, 3333–3349, https://doi.org/10.1175/JAS-D-22-0086.1, 2022.

Saito, M., Yang, P., Ding, J., and Liu, X.: A Comprehensive Database of the Optical Properties of Irregular Aerosol Particles for Radiative Transfer Simulations, J. Atmospheric Sci., 78, 2089–2111, https://doi.org/10.1175/JAS-D-20-0338.1, 2021.

Schladitz, A., Müller, T., Kaaden, N., Massling, A., Kandler, K., Ebert, M., Weinbruch, S., Deutscher, C., and Wiedensohler, A.: In situ measurements of optical properties at Tinfou (Morocco) during the Saharan Mineral Dust Experiment SAMUM 2006, 61, 64, https://doi.org/10.1111/j.1600-0889.2008.00397.x, 2009.

Schmid, O., Artaxo, P., Arnott, W. P., Chand, D., Gatti, L. V., Frank, G. P., Hoffer, A., Schnaiter, M., and Andreae, M. O.: Spectral light absorption by ambient aerosols influenced by biomass burning in the Amazon Basin. I: Comparison and field calibration of absorption measurement techniques, Atmospheric Chem. Phys., 6, 3443–3462, https://doi.org/10.5194/acp-6-3443-2006, 2006.

Sokolik, I., Andronova, A., and Johnson, T. C.: Complex refractive index of atmospheric dust aerosols, Atmospheric Environ. Part Gen. Top., 27, 2495–2502, https://doi.org/10.1016/0960-1686(93)90021-P, 1993.

Sorribas, M., Olmo, F. J., Quirantes, A., Lyamani, H., Gil-Ojeda, M., Alados-Arboledas, L., and Horvath, H.: Role of spheroidal particles in closure studies for aerosol microphysical–optical properties, Q. J. R. Meteorol. Soc., 141, 2700–2707, https://doi.org/10.1002/qj.2557, 2015.

Stegmann, P. G. and Yang, P.: A regional, size-dependent, and causal effective medium model for Asian and Saharan mineral dust refractive index spectra, J. Aerosol Sci., 114, 327–341, https://doi.org/10.1016/j.jaerosci.2017.10.003, 2017.

Sun, L.-H., Bi, L., and Yi, B.: The Use of Superspheroids as Surrogates for Modeling Electromagnetic Wave Scattering by Ice

815   Crystals, Remote Sens., 13, 1733, https://doi.org/10.3390/rs13091733, 2021.

Takemura, T., Okamoto, H., Maruyama, Y., Numaguti, A., Higurashi, A., and Nakajima, T.: Global three-dimensional simulation of aerosol optical thickness distribution of various origins, J. Geophys. Res. Atmospheres, 105, 17853–17873, https://doi.org/10.1029/2000JD900265, 2000.

Tegen, I. and Fung, I.: Modeling of mineral dust in the atmosphere: Sources, transport, and optical thickness, J. Geophys. Res.

820   Atmospheres, 99, 22897–22914, https://doi.org/10.1029/94JD01928, 1994.

Virkkula, A., Mäkelä, T., Hillamo, R., Yli-Tuomi, T., Hirsikko, A., Hämeri, K., and Koponen, I. K.: A Simple Procedure for Correcting Loading Effects of Aethalometer Data, J. Air Waste Manag. Assoc., 57, 1214–1222, https://doi.org/10.3155/1047-3289.57.10.1214, 2007.

Volz, F. E.: Infrared Refractive Index of Atmospheric Aerosol Substances, Appl. Opt., 11, 755–759,

825   https://doi.org/10.1364/AO.11.000755, 1972.

Wagner, R., Ajtai, T., Kandler, K., Lieke, K., Linke, C., Müller, T., Schnaiter, M., and Vragel, M.: Complex refractive indices of Saharan dust samples at visible and near UV wavelengths: a laboratory study, Atmospheric Chem. Phys., 12, 2491–2512, https://doi.org/10.5194/acp-12-2491-2012, 2012.

Wang, Z., Bi, L., Jia, X., Yi, B., Lin, X., and Zhang, F.: Impact of Dust Shortwave Absorbability on the East Asian Summer

830   Monsoon, Geophys. Res. Lett., 47, e2020GL089585, https://doi.org/10.1029/2020GL089585, 2020.

Wang, Z., Bi, L., Wang, H., Wang, Y., Han, W., and Zhang, X.: Evaluation of a new internally-mixed aerosol optics scheme in the weather research and forecasting model, J. Quant. Spectrosc. Radiat. Transf., 283, 108147, https://doi.org/10.1016/j.jqsrt.2022.108147, 2022.

Wang, Z., Bi, L., and Kong, S.: Flexible implementation of the particle shape and internal inhomogeneity in the invariant

835   imbedding T-matrix method, Opt. Express, 2023."accepted"

Weingartner, E., Saathoff, H., Schnaiter, M., Streit, N., Bitnar, B., and Baltensperger, U.: Absorption of light by soot particles: determination of the absorption coefficient by means of aethalometers, J. Aerosol Sci., 34, 1445–1463, https://doi.org/10.1016/S0021-8502(03)00359-8, 2003.

Wells, K. C., Martins, J. V., Remer, L. A., Kreidenweis, S. M., and Stephens, G. L.: Critical reflectance derived from MODIS:

840   Application for the retrieval of aerosol absorption over desert regions, J. Geophys. Res. Atmospheres, 117, https://doi.org/10.1029/2011JD016891, 2012.

Yang, P. and Liou, K. N.: Geometric-optics–integral-equation method for light scattering by nonspherical ice crystals, Appl. Opt., 35, 6568–6584, https://doi.org/10/fgfdnq, 1996.

Yang, P., Feng, Q., Hong, G., Kattawar, G. W., Wiscombe, W. J., Mishchenko, M. I., Dubovik, O., Laszlo, I., and Sokolik, I.

845   N.: Modeling of the scattering and radiative properties of nonspherical dust-like aerosols, J. Aerosol Sci., 38, 995–1014, https://doi.org/10.1016/j.jaerosci.2007.07.001, 2007.

Yu, J., Bi, L., Han, W., and Zhang, X.: Application of a Neural Network to Store and Compute the Optical Properties of Non-Spherical Particles, Adv. Atmospheric Sci., https://doi.org/10.1007/s00376-021-1375-5, 2022.

Zong, R., Weng, F., Bi, L., Lin, X., Rao, C., and Li, W.: Impact of hematite on dust absorption at wavelengths ranging from

850   0.2 to 1.0 µm: an evaluation of literature data using the T-matrix method, Opt. Express, 29, 17405–17427, https://doi.org/10.1364/OE.427611, 2021.